

1
2
3
4
5
6
7
8
9
10
11
12
13
14
15
16
17
18
19
20

TIME-DEPENDENT FLEXURAL BEHAVIOUR OF CRACKED STEEL FIBRE REINFORCED SELF-COMPACTING CONCRETE PANELS

Amin Abrishambaf ^{*1}, Joaquim A. O. Barros¹ and Vitor M.C.F. Cunha¹

¹ ISISE, Dep. Civil Eng., School Eng., University of Minho, Campus de Azurém 4800-058 Guimarães, Portugal

ABSTRACT

In the present work are described and discussed the results of an extensive experimental program that aims to study the long-term behaviour of cracked steel fibre reinforced self-compacting concrete, SFRSCC, applied in laminar structures. In a first stage, the influence of the initial crack opening level ($w_{cr} = 0.3$ and 0.5 mm), applied stress level, fibre orientation/dispersion and distance from the casting point, on the flexural creep behaviour of SFRSCC was investigated. Moreover, in order to evaluate the effects of the creep phenomenon on the residual flexural strength, a series of monotonic tests were also executed. It was found that $w_{cr} = 0.5$ mm series showed a higher creep coefficient comparing to the series with a lower initial crack opening. Furthermore, the creep performance of the SFRSCC was influenced by the orientation of the extracted prismatic specimens regarding the direction of the concrete flow within the cast panel.

Keywords: Long-Term Performance; Creep; Tensile Properties; Rheology; Fibre Reinforcement.

* Author to whom the correspondence should be sent (abrishambaf@civil.uminho.pt)
Tel: +351 253 510 210 Fax: +351 253 510 217

1 1. INTRODUCTION

2 Discrete fibres are increasingly being used in the construction industry to overcome the brittle nature of plain
3 concrete under tension, and either to avoid or reduce the use of conventional steel reinforcement. In fibre reinforced
4 concrete, FRC, macro-cracks that arise within the cementitious matrix are bridged by fibres randomly distributed in
5 the concrete. The fibres are able to transfer the stresses across the crack's surfaces improving the tensile post-
6 cracking strength that enhances the composite's toughness and crack growth control, resulting favourable effects in
7 terms of load carrying capacity, ductility and durability of structures made by FRCs. It has been investigated
8 extensively that mechanical properties of steel fibre reinforced concrete, SFRC, depend on both the fibre orientation
9 and distribution [1-3]. Moreover, discrete fibres are more effective when preferentially aligned along the directions
10 of the principal tensile stresses.

11 The effectiveness of a fibre as a reinforcing element becomes more predominant after has been crossed by a crack.
12 Determination of the tensile post-cracking behaviour of SFRC has been widely studied, either by direct or indirect
13 tests [4-8]. However, regarding the long-term response of this composite, the available knowledge in literature is
14 still somehow quite scarce.

15 The creep deformation of the material could ultimately lead to the failure mechanism of the structural element at a
16 lower load than static ultimate load [9]. On the other hand, in some structural systems, the long-term deformation of
17 the structural element can be beneficial, since it enforces stresses to redistribute, which can limit the crack
18 propagation. From another point of view, if the creep deformation damages significantly affect the fibre/matrix
19 interface bond, it will lead to an undesirable excessive decrease on the post-cracking strength, thus the influence of
20 creep will be adverse [10]. Some information is available in literature regarding to the time-dependent behaviour of
21 FRC in the cracked state [10-14]. However, many of them mainly assessed the creep behaviour of concrete
22 reinforced with synthetic fibres [15-17]. It was reported that the cracked micro/macro-synthetic fibre reinforced
23 concrete presented significant crack widening over time under sustained uniaxial tensile load [9, 18]. There are also
24 some works regarding the creep evaluation of steel fibre reinforced concrete under uniaxial tensile loading [19, 20]
25 and flexural loading [10, 14]. It was showed that application of steel fibres in concrete limited long-term crack
26 widening considerably [13, 21]. It is worth noting that focus of the mentioned studies was principally on the beams

1 where, in the case of using steel fibre reinforced self-compacting concrete, the rotation of the fibres due to the
2 concrete flow was completely distinct of planar structures [22, 23].

3 Creep in bending of a cracked SFRC element is the result of the following phenomena: concrete creep in
4 compression (produce basic creep); fibres creep at material level in tension; loss of fibre-matrix adherence and
5 subsequent fibre free-sliding. Creep of fibres is only significant in fibres susceptible to thermo-hygrometric effects,
6 not in the case of the steel fibres. It was shown that the time dependent alterations in the fibre and matrix interface
7 zone influence significantly the long-term fibre reinforcement effectiveness, and, consequently, the creep behaviour
8 of cracked fibre reinforced concrete [9, 18]. The crack width opening and progression with time are strongly
9 dependent of the long-term behaviour of concrete, load and environmental conditions. Therefore, it is important to
10 evaluate the concrete capability to maintain the crack opening width relatively low under a sustained load, in order
11 to guarantee the effectiveness of fibres under serviceability conditions. Moreover, despite being available some
12 standards for designing SFRC structures [24, 25], it seems that they still not take into account the long-term
13 behaviour under cracked conditions. Therefore, information regarding the long-term behaviour of cracked SFRC
14 elements, particularly planar structures, is still limited. Consequently, understanding the behaviour of cracked SFRC
15 elements under a sustained load will help towards a more rational design and accurate prediction of the composite
16 behaviour under serviceability conditions.

17 In the present work an extensive experimental program that aims to study the long-term behaviour of cracked steel
18 fibre reinforced self-compacting concrete, SFRSCC, is described. For this purpose, prismatic specimens were
19 extracted from a SFRSCC panel cast from its centre, and the relevant results obtained from the creep tests with these
20 specimens are presented and discussed. The influence of fibre orientation and dispersion on the creep behaviour of
21 cracked SFRSCC elements was appraised. This was achieved based on the angle between the extracted specimen's
22 notch plane and the expected concrete flow direction, since extracted specimens were notched in distinct directions.
23 The prismatic specimens were previously subjected to a four-point bending test up to a certain crack width opening
24 ($w_{cr} = 0.3$ and 0.5 mm). Then the bending test was carried out under a sustained load until the stabilization of the
25 crack width opening. In a first stage the influence of the initial crack opening level, applied stress level [50-100%],
26 fibre orientation/dispersion, and distance from the casting point on the flexural creep behaviour was investigated.
27 Afterwards, the specimens used in the flexural creep tests were subjected to an instantaneous four-point bending test
28 until failure. Finally, a series of instantaneous four-point bending tests were also executed on uncracked prismatic

1 specimens, in order to quantify the influence of the creep phenomenon on the evolution of the flexural residual
2 strength.

3 **2. EXPERIMENTAL PROGRAM**

4 **2.1. Concrete mixture**

5 A SFRSCC was produced according to the mixture composition given in Table 1. W/C abbreviates water (W) to
6 cement (C) ratio. Superplasticizer Sika® 3005 (SP) has been used to assure the required self-compactibility
7 requirements due to the low water content. A crushed granite coarse aggregate was used with a maximum aggregate
8 size of 12 mm. A fibre content of 60 kg/m³ of hooked-end steel fibres was used. The fibres had the following
9 characteristics: 33 mm of length, l_f ; 0.55 mm of diameter, d_f ; aspect ratio, l_f/d_f , of 60 and a yield stress of about
10 1100 MPa. The fresh concrete behaviour was determined by the Abrams cone slump test in the inverted position
11 according to EFNARC recommendations [26]. The spread diameter was approximately 590 mm.

12 The SFRSCC's compressive strength was assessed by testing 6 cylinders with a diameter of 150 mm and a height of
13 300 mm. After casting, the specimens were stored in a climatic chamber room at constant temperature of 20 °C and
14 relative humidity of 60%. The cylinders were tested at the age of 28 days, and an average compressive strength and
15 an average young modulus of 72 MPa and 42.15 GPa was obtained, respectively, with a coefficient of variation
16 (CoV) of 8.23% and 0.26%, respectively.

17 **2.2. Specimens**

18 The panel represents the outer layers of a sandwich panel conceived under the framework of a research project for
19 the development of modular prefabricated affordable houses [27, 28]. The casting of this panel for the SFRSCC
20 cracked creep tests was performed from its geometrical centre. However, previous research has revealed that this
21 casting procedure improves the residual tensile behaviour since due to the circular distribution of fibres through the
22 panel, a higher number of effective fibres exist in order to bridge the radial cracks formed when the panel was
23 loaded from its centre [29]. The fresh concrete was poured directly from a mixing truck by a U-shape channel

1 almost in the vertical position into a mould with the dimensions of $1500 \times 1500 \text{ mm}^2$ in plan and 60 mm of
2 thickness. A total of one hundred and twelve prismatic specimens with the dimensions of $240 \times 60 \times 60 \text{ mm}^3$ were
3 extracted from distinct locations of the panel. The orientation of the extracted prismatic specimens within the panel
4 was established having in mind the expected concrete flow direction, see Fig. 1(a). In this scheme, the light grey
5 solid hatched specimens were used for assessing the long-term behaviour, whereas the rest of the specimens were
6 tested under instantaneous monotonic load conditions at the same age of the specimens cracked for the creep test.
7 Since the panel was cast in its centre point, the symmetry of the panel assures that for each specimen in the creep
8 test, there will be a mirror specimen on the other side of the panel for the execution of the monotonic test to estimate
9 the effects of creep crack width propagation on the residual strength. For instance, in Fig. 1(a), specimen L-7.5°-8
10 was tested under monotonic load condition while specimen L-0.5-7.5°-5 was used for the creep test. After the
11 extraction of the prismatic specimens, a notch was executed at its middle length. The notch depth and thickness were
12 10 and 2 mm, respectively.

13 The influence of the crack plane orientation towards the expected concrete flow was assessed in four different
14 directions. The orientation of the notched plane was defined accordingly to the following strategy: by considering β
15 as the angle between the direction of the concrete flow and the notched plane direction, four series of prismatic
16 specimens with different notched plane orientations towards the concrete flow directions can be defined (Fig. 1b).
17 Fig. 1 depicts a scheme of the adopted classification methodology based on the angle β . The four intervals
18 established for the angle β were $[0-15^\circ]$, $[15-45^\circ]$, $[45-75^\circ]$ and $[75-90^\circ]$. Since in previous research [1] it was found
19 that the radial flow of the SFRSCC promotes a preferential fibre alignment perpendicularly to the flow direction, the
20 present adopted strategy enables to appraise the influence of fibre orientation, at a certain distance from the casting
21 position, on the instantaneous force-crack width ($\sigma-w$) and on the creep coefficient-time ($\phi-t$) relationships.
22 Hereinafter, each series was designated by an alphanumeric string according to: in the case of the specimens for the
23 long-term tests, the first character represents the distance from the casting point (L-Low: $[0-375\text{mm}]$; A-Average:
24 $[375-565 \text{ mm}]$ and H-High: $[565-750 \text{ mm}]$); the second numeral refers to the two studied pre-crack widths (w_{cr}), 0.3
25 and 0.5 mm; the third numeral defines the β angle, in degrees, for four intervals of the relative orientation between
26 the notched plane and the SFRSCC flow lines (7.5: $[0-15^\circ]$, 30: $[15-45^\circ]$, 60: $[45-75^\circ]$ and 87.5: $[75-90^\circ]$), and the
27 last numeral represents the number of the series' specimen. For instance, L-0.3-7.5°-1 represents the specimen
28 number 1 located at a low distance from the casting point, with a pre-crack width of 0.3 mm, and with an angle β in

1 the [0-15°[interval. A similar strategy for the designation of the instantaneous monotonic test specimens was
2 followed, however the second character that indicates the pre-crack width was ignored, since these tests were
3 performed on uncracked specimens in opposition to the creep tests.

4 **2.3. Test setup**

5 **2.3.1. Monotonic four-point bending test**

6 The instantaneous F -CTOD (crack tip opening displacement) relationship representative of the SFRSCC panel was
7 determined with a total of sixty four monotonic four-point bending tests. These tests were carried out on notched
8 beams extracted from the panel following the recommendations of Italian standard [25]. The monotonic tests were
9 carried out on a universal testing machine of 50 kN load bearing capacity and at a displacement rate of 0.002 mm/s.

10 Fig. 2 depicts the test setup and geometry of the specimen. To determine the deflection during the test, a LVDT
11 (Linear Variable Differential Transformers) was mounted on an aluminium bar supported at mid height of the
12 sections coinciding with the supports of the specimen in order to exclusively record the deflection of the specimen,
13 see Fig. 2(a). In order to follow the recommendations of UNI 11039 [25] this lateral face of the specimen coincides
14 with the surface of the SFRSCC panel in contact with the mould, and the notch was executed in the face parallel to
15 the casting direction. Therefore the bottom face of the specimen in the test setup corresponds to a lateral surface of
16 the extracted beam from the panel, i.e. the beam was rotated 90° along its longitudinal axis for testing. To assess an
17 eventual asymmetric crack opening, due to fibre segregation along the panel's thickness, CTOD was measured by
18 installing three LVDTs on the beam's bottom surface, see Fig. 2(b). These transducers recorded the crack opening
19 width at about 10 mm from the top and bottom surfaces of the panel, as well as at its middle height. The adopted
20 disposition of the aluminium LVDT supports mitigates the measurement of the elastic deformations surrounding the
21 mouth of the notch plane, see Fig. 2(c).

22

23 **2.3.2. Long-term four-point bending tests**

24 In order to obtain the long-term F - w (crack width) relationship, experimental tests were carried out in three stages:
25 firstly, the beams were pre-cracked up to a crack width of either 0.3 or 0.5 mm; secondly, the creep tests were

1 carried out on the pre-cracked beams until the stabilization of the creep crack width has been achieved; finally, post-
2 creep bending tests were performed until failure of the specimen.

3

4 *2.3.2.1. Pre-cracking of the specimens*

5 The creep four-point bending tests were performed in pre-cracked specimens. Therefore, in a first stage, the
6 monotonic test set-up previously described was used to achieve the desired crack opening width (w_{cr}). In this
7 research, two initial crack opening widths were studied, namely, 0.3 mm, recommended for the serviceability limit
8 state, and 0.5 mm that is coincide to the crack opening width corresponding to the one used to compute the residual
9 flexural strength, $f_{R,1}$ [24]. Afterward, the test was stopped and the specimen unloaded.

10

11 *2.3.2.2. Creep test*

12 After finalizing the pre-cracking procedure, the specimens were carefully moved to the climate chamber room, at a
13 temperature of $20^{\circ}\text{C} \pm 0.5$ and a 60% relative humidity $\pm 5\%$. The creep testing rigs were located inside this room,
14 thus the creep tests were carried out under controlled thermo-hygro-metric conditions. The creep testing rig allowed
15 to simultaneously loading three specimens. Fig. 3(a) shows the adopted creep test set-up. Before mounting the
16 specimens in the creep testing frame, they were kept in the chamber room for five hours to acclimatize. The test was
17 executed under force control. Specimens were loaded by injecting oil into the hydraulic actuator until the desired
18 value of the load has been reached. The specimens' loading procedure was carried out very carefully in order to
19 attain the target load level with the minimum deviation as possible. To measure the crack opening width, for each
20 specimen, one LVDT was installed at the middle of the notched surface, see Fig. 3(b). The LVDTs and load cell
21 were connected to a computerized data acquisition system. The data was recorded in distinct time-steps according to
22 the following procedure: during loading and unloading of specimen: one sample per 5 seconds; in the first and
23 second month after loading: one sample per 500 seconds and one sample per 1000 seconds, respectively.

24 After the initiation of the creep test, the value of the applied load, F_a , was fixed and maintained constant until the
25 crack opening width was stabilized. When the variation of the crack opening value was smaller than one micrometer
26 for three consecutive days, it was assumed that the crack opening was stabilized, and then the test was finalized. In

1 the present research, for each creep frame, beams were positioned and loaded according to the following
2 methodology: the beam with the highest value of F_{cr} (the load corresponding to w_{cr}) was placed on the bottom, with
3 a moderate F_{cr} was localized in the middle, and with the lowest F_{cr} was placed on the top. Then, they were loaded
4 simultaneously with the smallest F_{cr} value of these three tested specimens. In other words, it was opted to apply a
5 load level that produces a bending moment in the notched cross section of the beam placed on top of the frame equal
6 to 100% of that observed at $w_{cr}=0.3$ or 0.5 mm in the pre-cracking test. By following this methodology, the
7 influence of different loading levels (F_a / F_{cr}) on the long-term behaviour of the adopted SFRSCC could be
8 investigated as well.

9 Afterward the conclusion of the creep tests, the specimens were unloaded, but the data acquisition system was kept
10 active for at least a period of one week, enabling to record the closing of the crack width due to the creep recovery
11 process. Fig. 4(a) and (b) show schematically the variation of crack opening versus time and force-crack opening
12 relationship, respectively. In these figures, w_{inst} is the instantaneous crack opening, w_{lt} is the long-term crack
13 opening, w_{inst}^{rec} is the instantaneous crack opening recovery at the beginning of unloading process, w_{lt}^{rec} represents
14 the long-term crack opening recovery, w_{total}^{rec} is total crack opening recovery, w_{lt}^{res} indicates the residual crack opening
15 after unloading stage, and F_a depicts applied load level in creep test.

16

17 2.3.2.3. Post-Creep test

18 After the end of the creep tests and one week waiting period in order to enable creep deformation recovery, the
19 specimens were then subjected to monotonic four-point bending tests until a 4 mm crack mouth opening width has
20 been reached. The monotonic test set-up was similar to the one used for pre-cracking the beams, which was
21 previously presented. A same displacement rate of 0.002 mm/s was also implemented.

22

23 2.3.2.4. Assembled long-term force-crack width curve

24 Finally, the complete $F-w$ curves were assembled with the individual $F-w$ curves from the pre-cracking, creep and
25 post-creep responses, as shown in Fig. 5. The push curve from this assembled response will be compared with the
26 correspondent curve from the monotonic test on uncracked beams. In Fig. 5, hereinafter, F_L is the load at crack

1 initiation, F_{cr} and w_{cr} are the load and correspondent crack opening, respectively, for the defined pre-crack levels, i.e.
2 0.3 and 0.5 mm, w_{cr}^{res} is the residual crack opening after unloading of the specimen, K_{sec} is secondary stiffness at re-
3 loading process of post-creep test, F_p^{max} and w_p^{max} are the maximum load at post-cracking branch and its
4 correspondent crack opening width, respectively.

5

6 **2.4. Assessment of fibre orientation and distribution**

7 The distribution and orientation of fibres in the SFRSCC panel was assessed by an image analysis procedure. The
8 adoption of this strategy was mainly due to its simplicity and relatively low cost [3, 30, 31]. The image analysis was
9 carried out on a plane parallel to the notch plane with an offset equal to half the length of the used fibre (Fig. 6). The
10 grinded plane was obtained by cutting the specimens after the monotonic four-point (4-P) bending tests have been
11 carried out. For each series ($\beta=[0-15^\circ]$, $[15-45^\circ]$, $[45-75^\circ]$ and $[75-90^\circ]$) five specimens from distinct panel locations
12 were selected. After computation and analysis of the image technique results, the following parameters that
13 characterize the fibre structure were derived out:

- 14 1. The number of fibres per unit area, N^f ;
- 15 2. Fibre orientation factor, η_θ ;
- 16 3. Fibre segregation parameter, ξ_{seg} ;

17 More details regarding the image analysis method and also on the process of the evaluation of the abovementioned
18 parameters can be found in appendix A. Furthermore, the number of the effective fibres per unit area, N_{eff}^f , was also
19 determined. This parameter could not be assessed through the previous technique, therefore it was appraised by
20 manually counting the fibres that intersected the notched plane of the tested beams and also had the hooked end
21 deformed (in order to be considered a fibre that provided effective reinforcement).

1 3. RESULTS AND DISCUSSION

2 3.1. Fibre orientation and distribution

3 Table 2 includes the fibre distribution parameters obtained by an image analysis technique. N^f and N_{eff}^f were higher
4 in the specimens with the notched plane parallel to the expected concrete flow direction, confirming the results
5 already obtained in this respect [1]. In general, these values decreased as the notched plane rotated towards to the
6 perpendicular position regarding the flow direction (Fig. 7). For the case of the notched plane orientation, β ,
7 comprised within $[0-15^\circ[$, N_{eff}^f was approximately 76, 156 and 686% higher than when β was between $[15-45^\circ[$,
8 $[45-75^\circ[$ and $[75-90^\circ]$ intervals, respectively. Regarding to the low value of N_{eff}^f compared to N^f it should be
9 mentioned that due to the high compressive strength of the concrete which exist a strong bond between fibre and
10 matrix, many of fibres were ruptured during the execution of monotonic test. Since in the determination of N_{eff}^f
11 only fibres with mobilized hook were counted and the ruptured fibres were not taken in to the account, this
12 parameter revealed a lower value.

13 Moreover, considering the fibre orientation factor, η_θ , a similar trend to the one obtained for the number of fibres
14 was found. A quite higher η_θ value was achieved for the series with a $\beta=[0-15^\circ[$, having been 8, 20 and 30% higher
15 than the one obtained for the series $[15-45^\circ[$, $[45-75^\circ[$ and $[75-90^\circ]$, respectively. This could be ascribed to a
16 preferential fibre alignment, which was influenced by the flowability of concrete, and induces the fibres to be
17 reoriented and remain preferentially perpendicular to the concrete flow direction. The fibre segregation parameter,
18 ξ_{seg} , can assume values between 0 (segregation at the top of the cross-section) and 1 (segregation at the bottom of
19 the cross-section). In a SFRC with homogeneous fibre distribution, ξ_{seg} is 0.5. From the results in Table 2 it is
20 verified the occurrence of a slight segregation of the fibres of similar level for all the series considered, caused by
21 the highest specific weight of the steel fibres amongst the constituents of the SFRSCC. However, this segregation
22 was lower than the one reported when SFRC is cast with mechanical vibration, since this operation is not executed
23 in SFRSCC.

1 According to the obtained results, in the case of casting panels, and in particular from its centre, since the wall
2 effects were limited mainly to the bottom surface, the flow velocity was uniform and diffused radially outwards
3 from the centre casting point, see Fig. 7(a). As a consequence, in the specimens with the notched plane direction
4 parallel to the flow direction, a higher number of effective fibres was observed, than when the specimens had the
5 notched plane perpendicular to the expected flow direction. Fig. 7(b) shows the influence of the concrete flow
6 velocity profile on the preferential orientation of the fibres along the thickness of the panel. According to the
7 expected concrete flow velocity profile, due to friction between concrete and the bottom surface of the panel (wall
8 effect), the flow velocity starts to decrease nonlinearly from the top to bottom panel's face. Therefore, fibres tend to
9 be more aligned in horizontal planes parallel to the bottom surface of the panel.

10 Fig. 8 illustrates the orientation probability density functions obtained for the average fibre orientation factor of each
11 series separately, ($\beta=[0-15^\circ[, [15-45^\circ[, [45-75^\circ[$ and $[75-90^\circ]$), as well as the orientation probability functions for
12 both the two and three-dimensional isotropic uniform random distributions. In this figure, the distribution of the
13 orientation angle through the cut plane was investigated for each specimen and the experimental results were
14 compared to Gaussian distribution. According to this study, the distribution of the orientation angle follows closely a
15 Gaussian distribution [32]. Fig. 8(a) presents the distribution of the probability of fibre orientation for the specimens
16 comprised in the interval $\beta=[0-15^\circ[$, which was shifted to the left side, meaning that fibres have a tendency to be
17 aligned more perpendicular to the notched plane. When angle β increases, which is translated in a reduction of the
18 orientation factor, the distribution was shifted from the left to the right side progressively, see Figs. 8(b) to 8(d).
19 Comparing the theoretical orientation factor for a two-dimensional fibre distribution, $2/\pi$ [33], and a three-
20 dimensional, 0.5 [34], isotropic uniform random fibre distribution with the orientation factors for the distinct β
21 series, it was observed that the $[0-15^\circ[$ series showed a completely different distribution. As the value of β increased,
22 the fibre distribution within the panels tended to a two-dimensional distribution. Fig. 8(d) shows that the orientation
23 distribution of the $[75-90^\circ]$ series almost coincided with two-dimensional fibre distribution. Consequently, when a
24 SFRSCC panel was cast from the centre, assuming a two-dimensional distribution could be far apart from the
25 reality. Therefore, in SFRSCC panels, mainly, due to the high flowability of the self-compacting concrete, it was
26 expected an anisometric fibre structure. Hence, since the material tensile behaviour of fibre reinforced concretes was
27 intimately connected to the fibre distribution, an anisotropic material behaviour should be considered. In conclusion,

1 in the present case, the fibre distribution was prominently influenced by the placing conditions and concrete
2 flowability.

3 **3.2. Monotonic four-point bending test**

4 Fig. 9(a) to (d) depicts the envelope and average force-crack mouth opening displacement relationships, F -CTOD,
5 obtained from the monotonic four-point bending tests when β =[0-15°[, [15-45°[, [45-75°[and [75-90°], respectively.
6 The CTOD was determined by averaging the displacements recorded in the three LVDTs fixed at the bottom face of
7 the specimen (Fig. 2). The recorded value of crack opening width ($CMOD_y$) was corrected to the real crack tip
8 opening width (CTOD) as follows:

$$9 \quad CTOD = CMOD_y \frac{h}{h + y} \quad (1)$$

10 where, $CMOD_y$ is the recorded value in the LVDTs at a distance y below the notch mouth of the specimen, and h is
11 the total depth of the specimen.

12 In general, the specimens have shown a linear behaviour up to the load correspondent to the crack initiation. Up to
13 this load, the value measured by the LVDTs corresponds to the elastic deformation of the SFRSCC bulk in-between
14 the LVDT's supports (Fig. 2c). Therefore, the results exhibited a low scatter, since in this stage, the contribution of
15 the fibres was almost null as the material response was mainly dependent on the elastic behaviour of the concrete
16 constituents. After the cracking onset, the fibres started to be mobilized bridging the stresses across the crack
17 surfaces. In general, for the post-cracking stage the scatter was relatively high, because after the mobilization of
18 fibres the composite performance was extremely dependent of the fibre dispersion and orientation. Since the beams
19 were extracted from different locations of the panel at distinct distances from the casting point, a high scatter of the
20 tests results was expected. This aspect can be ascribed to the reduction of the concrete flow velocity with the
21 increase of the distance to the casting point.

22 Regarding the first two series, namely, β =[0-15°[and [15-45°[, they have shown a similar force value at the limit of
23 proportionality. Once the tensile strength of material was attained, both series revealed a deflection-hardening
24 response up to a CTOD of around 0.6 mm, but for [15-45°[specimens a slightly lower peak load value was attained.
25 From the micromechanical point of view, after the adhesion of fibre and surrounding matrix has been exceeded, the

1 fibre reinforcement effectiveness was mainly governed by the plastification process of the hooked end, which
2 provides the highest contribution for this deflection-hardening capacity. Afterward, a softening stage was observed
3 for both series. In the $\beta=[0-15^\circ]$ case, since the specimens contained more fibres that intersected the cracked plane
4 with a lower angle, i.e. 29° , the residual force decay was smoother, whereas for the $\beta=[15-45^\circ]$ series, a higher load
5 decay was observed between 0.74 and 1.5 mm of CTOD. In the latter specimens, fibres have intersected the cracked
6 plane with a higher average orientation angle, i.e. 36° , see Fig. 8(b). Fibre pull-out tests carried out have shown that
7 fibres with an orientation angle of 30° ruptured for a slip value nearby 0.5 mm [35]. Therefore, in this series, once
8 the peak load was attained, the fibres are more prone to be ruptured within the CTOD range of 0.74-1.5 mm.
9 Actually, during the execution of the test, the strident sound of the fibres rupturing was clearly differentiated.

10 Regarding the cases of $\beta=[45-75^\circ]$ and $[75-90^\circ]$ series, after the crack initiation, the load decreased suddenly,
11 followed by a small plateau, and beyond a CTOD of about 0.75 mm the load decreased smoothly. This could be
12 ascribed to a higher probability of fibre rupture [35], since in these two series, fibres have a tendency to be oriented
13 with a higher orientation angle towards the notched plane, see Fig. 8(c) and (d), with average orientation angles of
14 43° and 48° , respectively.

15 By comparing all F -CTOD relationships, Fig. 9(e), could be concluded that the post-peak behaviour of the SFRSCC
16 was highly dependent of the direction in which the mechanical properties were assessed. The series with the notched
17 plane more parallel towards to the concrete flow direction, i.e. $[0-15^\circ]$ and $[15-45^\circ]$ series, showed a higher residual
18 force, and therefore a larger energy absorption capacity than the specimens with a fracture surface more
19 perpendicular to the flow direction. Further details and discussion of this aspect could be found elsewhere [1, 36].

20 **3.3. Long-term four-point bending test**

21 **3.3.1. Creep parameters**

22 Fig. 10 shows the relationship between the crack opening rate, COR, [$\mu\text{m}/\text{day}$] and the applied load level (F_a / F_{cr})
23 for the two pre-crack widths investigated (i.e. 0.3 and 0.5 mm). The crack opening rate was determined from Eq. (2)
24 at 7, 15, 30 and 60 days.

$$COR_{t_2-t_1} = \frac{w_{lt}^{t_2} - w_{lt}^{t_1}}{t_2 - t_1} \quad (2)$$

where $COR_{t_2-t_1}$ is the crack opening rate between time t_2 and t_1 , and $w_{lt}^{t_i}$ is the long-term crack opening at time t_i (Fig. 4). For both $w_{cr}=0.3$ and 0.5 mm series, at 7 and 15 days, the COR increased with the load level. This increase of COR was more significant in the $w_{cr}=0.5$ mm series and for F_a / F_{cr} ratios higher than 80%. Considering the COR evolution with F_a / F_{cr} in the first two weeks of loading, it was observed for $w_{cr}=0.3$ mm a linear trend, while for $w_{cr}=0.5$ mm it was detected a nonlinear increase of the COR with F_a / F_{cr} . In the case of $F_a / F_{cr} = 100\%$, COR was in average 50% higher for the larger pre-cracking width, i.e. $w_{cr}=0.5$ mm. The COR at 30 and 60 days' time was not significantly influenced by the F_a / F_{cr} ratio since, in generally, after a period of one month the crack opening width tended to become stabilized.

To consider the long-term crack opening and also to take into account the loading levels of the specimens, the creep coefficient parameter in the creep stage (ϕ^C) is introduced, as being calculated by the following equation [37]

$$\phi^C = \frac{w_{lt}}{w_{inst}} \quad (3)$$

where w_{inst} is the instantaneous crack opening at the time of loading, and w_{lt} represents the long-term crack opening (Fig. 4a).

Fig. 11 illustrates the variation of the creep coefficient for different ratios of F_a / F_{cr} . As it was expected, this coefficient has increased with the load level ratio. Considering the influence of pre-crack width, the creep coefficient in $w_{cr} = 0.5$ mm series has increased with the F_a / F_{cr} at a higher rate than in the case of the series of $w_{cr}=0.3$ mm. By considering the micromechanical behaviour of a single fibre, the $w_{cr}=0.5$ series was submitted to higher damage level of fibre/matrix interface, which led to a higher increase of the crack opening width under a creep load. This influence was more meaningful for a load level of 100%. From the monotonic tests' results, see Fig. 9, it can be observed that the pre-cracking level of 0.5 mm was close to the CTOD correspondent to the maximum load at post-cracking branch, w_p^{\max} . Therefore, subjecting beams to a sustained load in a level near to the maximum bearing capacity load of the specimen at post-cracking branch, F_p^{\max} , can lead to a significant increase in the values of the creep coefficient. This was observed in the $w_{cr}= 0.5$ mm series at the higher load level.

1 In some specimens, during the reloading procedure of beams in the creep frame, a sudden increase in w_{inst} was
2 observed. This could be due to the rupturing of some fibres that were bridging the crack's surfaces. Since the matrix
3 had a high compressive strength, a strong bond between fibre and matrix interface was achieved. This influence was
4 more predominant for the series with $w_{cr}=0.5$ mm and $F_a/F_{cr}=100\%$ due to the previously explained reasons,
5 since the probability of fibre's rupturing is higher. For this series, larger creep coefficients and scatter were
6 expected, see Fig. 11. Regarding the $w_{cr}=0.3$ mm series, this was not observed, since the 0.3 mm crack width is still
7 far from w_p^{max} .

8 For the simplicity sake, it was decided to categorize the F_a/F_{cr} ratios into two distinct intervals [50-75%[and [75%-
9 100%] with an average values of 62.5 and 87.5%, designated as low and high grade F_a/F_{cr} ratios, respectively. Fig.
10 12 depicts the relationship between creep coefficient and time for the studied w_{cr} and F_a/F_{cr} ratios, up to a period of
11 two months. The creep curves were obtained by averaging the responses in each correspondent category. All series
12 showed a two-stage creep response, namely, the so-called primary and secondary stages. The creep coefficient
13 became stabilized within the studied time period, considering the criterion for stabilized creep, already indicated.
14 During the execution of the test, none of the beams entered into the tertiary creep stage, in which a specimen fails
15 due to creep. In general, the creep coefficient was approximately 48% and 64% higher for the high load level,
16 respectively, regarding $w_{cr}=0.3$ and 0.5 mm series. On the other hand, the influence of the pre-crack width on the
17 creep coefficient was smaller. Series with a $w_{cr}=0.5$ mm, loaded with a high F_a/F_{cr} ratio had 30% higher creep
18 coefficient than the one of the $w_{cr}=0.3$ mm series for the same level of loading. As explained earlier, this would be
19 feasible since $w_{cr}=0.5$ mm was close to w_p^{max} , in particular for the specimens with a load level of $F_a/F_{cr}=100\%$. It is
20 noteworthy that even in this case, a stable creep response was achieved.

21 It is should be mentioned that the measured long-term crack opening consists of two main phenomena: the basic
22 creep in the uncracked section under compression and time-dependent alterations between fibre and matrix
23 interface zone. However, for the specimens with proposed dimensions, the influence of the basic creep is
24 very negligible due to the following reasons: firstly, for the both studied pre-crack levels, where CTOD
25 reached to 0.3 or 0.5 mm, a major part of the section above the notch was cracked. On the other hand, the location of
26 the neutral axis was moved very close to the top of the specimen and thus, a small part of the section subjected to the
27 compressive stress. Secondly, the selected loads in the creep tests produced a very low compressive stress in the

1 section and if it compared with the concrete compressive strength which is relatively high, a very low basic creep
2 deformation is expected. Consequently, hereinafter, the long-term widening of the crack referred to the time-
3 dependent sliding action between fibre and surrounding matrix.

4 5 **3.3.2. Influence of distance from the casting point on the creep parameter**

6 Fig. 13 shows the influence of the specimens' distance to the casting point on the creep coefficient versus time
7 relationship for specimens with $F_a / F_{cr} = 100\%$. It was opted to only present these relationships for the maximum
8 F_a / F_{cr} , since they were considered as the most critical ones. Specimens positioned near the centre of the panel (i.e.
9 casting point) presented a lower creep coefficient, while those located in the corner of the panel had the highest
10 creep coefficients. This aspect could be ascribed to the decrease of the concrete flow velocity with the increase of
11 the distance from the casting point. This decrease of the flow velocity influences both the fibre dispersion and
12 orientation along the flow profile, and, consequently, leads to quite different fibre structures within the specimens at
13 distinct distances from the casting point. From another point of view, this observation could be also attributed to a
14 decrease of the matrix strength with the increase of the distance from the casting point due to some segregation of
15 the aggregate skeleton, resulting a weaker fibre/matrix interfacial bond strength that decreases the fibre
16 reinforcement effectiveness.

17 18 **3.3.3. Influence of notch plane orientation on the creep parameter**

19 Fig. 14 presents the influence of the notched plane orientation (regarded to the flow direction of SFRSCC) on the
20 relationship of creep coefficient versus time. These relationships were determined by averaging the response of the
21 specimens with $F_a / F_{cr} = 100\%$. For the $w_{cr} = 0.3$ mm series, the variation of creep with time was slightly affected
22 by the direction of the notched plane regarding the expected concrete flow, while in the $w_{cr}=0.5$ mm series this
23 influence was more significant. In the case of the $\beta=[0-15^\circ]$ series, the creep coefficient at the end of two months
24 was 13 and 31% higher than in $\beta=[75-90^\circ]$ for the $w_{cr}=0.3$ and 0.5 mm series, respectively. It is worth noting that
25 the $\beta=[0-15^\circ]$ specimens contain effective fibres perpendicular to the crack plane, which were pulled-out under a
26 sustain load progressively, while the $\beta=[75-90^\circ]$ specimens have fibres with a higher orientation angle towards the
27 notch plane. In this case, the fibre reinforcement mechanism of the specimen was mainly governed by matrix

1 spalling at the fibres' exit points instead of fibres pulled-out. Therefore, the development of creep coefficient along
2 time was influenced by the orientation of the crack plane within the SFRSCC panel, and this influence seems as
3 larger as higher is the crack width.

4 **3.4. Comparison between monotonic and long-term results**

5 Fig. 15 illustrates the relationship between long-term residual crack opening width, w_{lt}^{res} (Fig. 4), and secondary
6 stiffness in the re-loading of post-creep test, K_{sec} , (Fig. 5). It is observed that the stiffness of the re-loading branch of
7 the post-creep curve decreases with the increase of the long-term residual crack width. Furthermore, the following
8 equation was also proposed to estimate the influence of w_{lt}^{res} on the K_{sec} :

$$9 \quad k_{sec} = k_0 \left(\frac{c1}{(w_{lt}^{res})^{c2}} \right) \quad (4)$$

10 where K_0 is the initial stiffness determined by averaging the values obtained from force-CTOD relationships in Fig.
11 9 ($K_0=565.53$ kN/mm with a CoV of 12%), and constants $c1$ and $c2$ were achieved by nonlinear curve fitting
12 analysis procedures, having been obtained the following values: $c1=0.012$ and $c2=0.480$. Fig. 15 shows that Eq. (4)
13 fits with reasonable accuracy the obtained experimental results (R-square equal to 0.71).

14 Figs. 16 and 17 summarize the comparison between the long-term assembled curves (Fig. 5) obtained in four-point
15 bending tests and the correspondent ones determined in the monotonic tests, for $w_{cr} = 0.3$ and 0.5 mm, respectively.
16 These curves were obtained by averaging all responses. Regarding the monotonic tests, the experimental envelope
17 was also included. The long-term assembled curves consist of overlaying the force-CTOD curves from the tests
18 corresponding to: specimen's pre-cracking, creep, and post-creep. Moreover, each w_{cr} series was divided into eight
19 subcategories, according to the β orientation factor and the F_a / F_{cr} ratio. The results of the series $w_{cr}=0.3$ mm with a
20 low F_a / F_{cr} and $\beta=[75-90^\circ]$ were not presented (Fig. 16(g)), due to technical problems during the execution of the
21 tests of this series. From the analysis of these results, in general, it was concluded that the crack growth during the
22 creep tests has a minor influence on the post-creep flexural behaviour. In fact, it is evident that the assembled curves
23 resemble quite well the average response from the monotonic tests. Nevertheless, in some cases, due to the
24 scattering in the results, as consequence of distinct fibre distributions, the assembled responses did not follow so

1 closely the average monotonic curves, but nonetheless, they were yet comprised within the experimental envelope of
2 the monotonic flexural tests.

3 **4. ANALYTICAL APPROACH TO PREDICT CREEP BEHAVIOUR OF CRACKED SFRSCC**

4 In this section, the experimental results presented in section 3.3 were used to propose an equation to predict the
5 long-term response of the cracked SFRSCC. The influence of w_{cr} and F_a/F_{cr} parameters were taken into account in
6 the present approach. A combined power and hyperbolic equation was used, since similar equations were already
7 proposed by ACI 209-92 [38] and CEB (1999) [39] to predict creep behaviour of plain concrete. Therefore, the
8 following equation is proposed for predicting the long-term behaviour of cracked SFRSCC:

$$9 \quad \phi^c = \frac{t^A}{b + t^A} \quad (5)$$

10 where ϕ^c is creep coefficient, and t represents the time duration of loading (in hours). According to the
11 experimental data, for each w_{cr} , the coefficient A is determined by:

$$12 \quad A = w_{cr} \left(1 - 1 / (2F) \right) + d \quad (6)$$

13 Where w_{cr} is the pre-crack width (in mm) and F represents level of loading (F_a / F_{cr}). In Eqs. (5) and (6) the
14 constants b and d were determined by nonlinear curve fitting analysis procedures, and the following values were
15 obtained: $b=15$ (R-square value of 0.94) and $d=0.17$ (R-square value of 0.88). It should be mentioned that Eq. (5) is
16 only valid for $F_a / F_{cr} > 0.5$. Furthermore, the functions used may capture the shape of the phenomenon, but not
17 from their physical aspects. Fig. 18 compares the creep coefficient versus time obtained analytically and
18 experimentally for each series of different w_{cr} and loading level, where it was be concluded that the proposed
19 equation predicts with high accuracy the registered experimental data.

20 After determination of creep coefficient from Eq. (5), in order to determine the long-term crack opening analytically,
21 w_{lt} , Eq. (3) could be arranged as follows: $w_{lt} = \phi^c \times w_{inst}$. Figs. 19(a) and (b) depict the results of a parametric
22 study to investigate the influence of pre-crack width ($w_{cr} = 0.3$ and 0.5 mm) and also the load level ($F_a / F_{cr} = 0.5$,
23 0.6 , 0.7 , 0.8 , 0.9 and 1.0) on the long-term crack opening, w_{lt} , versus time response up to a period of one year. In this

1 study, since analytical determination of w_{inst} needs more experimental results, this parameter was determined using
2 experimental values for each studied w_{cr} and F_a / F_{cr} . However, it should be mentioned that to properly validate the
3 proposed equation for more generalized pre-crack widths, load levels, and higher time periods, more experimental
4 data is required. In general, the long-term crack opening increased with the increase of the F_a / F_{cr} ratio, and this
5 increase was more significant for higher values of w_{cr} . Considering now the influence of w_{cr} on the long-term crack
6 opening, for the same load level it was observed that the increase of w_{cr} lead to a significant increase of the long-
7 term crack opening, mainly for the higher load levels.

8 **5. CONCLUSIONS**

9 The present work reported the results of an experimental program to investigate the long-term behaviour of pre-
10 cracked SFRSCC laminar structures (of relatively small thickness). One hundred and twelve prismatic specimens
11 were extracted from a SFRSCC panel. These specimens were notched with different orientations regarding to the
12 expected SFRSCC flow direction, and were submitted to four-point flexural tests under a sustained load. The
13 influence of the following parameters on the creep behaviour was studied: initial crack opening level (0.3 mm and
14 0.5 mm), applied stress level, fibre orientation/dispersion, and distance from the casting point. Moreover, to evaluate
15 the effect of long-term crack opening on the flexural post-cracking strength, a series of instantaneous monotonic
16 tests were carried out and the corresponding force vs crack mouth opening displacement (F -CTOD) curves were
17 compared to the ones obtained by assembling the F -CTOD curves determined in pre-crack monotonic tests, creep
18 tests and post-creep monotonic tests.

19 From the monotonic tests, it was concluded that the post-cracking flexural tensile behaviour of the adopted SFRSCC
20 was considerably influenced by both the fibre dispersion and orientation. It is worthy to note that specimens with
21 notched plane parallel to concrete flow direction have shown the highest post-cracking strength. This was a direct
22 consequence of a preferential fibre orientation perpendicular to those fracture planes, due to the concrete flow
23 profile. Therefore, when a SFRSCC panel is cast from its centre, fibres tend to be aligned perpendicular to flow
24 direction.

25 Concerning the long-term creep tests, two pre-cracking levels (w_{cr}) were considered. Stable responses were observed
26 for all specimens. However, as it was expected, by increasing the level of the applied load, higher values of the

1 creep coefficient were achieved. Regarding the influence of the pre-cracking levels, $w_{cr}=0.5$ mm series conducted to
2 higher values of the creep coefficient than in the other studied series ($w_{cr}=0.3$ mm), especially, if they were loaded
3 with a high F_a / F_{cr} . On the other hand, since $w_{cr}=0.5$ mm was very close to the CTOD correspondent to the
4 maximum load at post-cracking branch of the monotonic responses, the bond interface between fibre and matrix was
5 more damaged, therefore the creep crack width increased with a higher rate. However, even in this case, still a stable
6 response was obtained, although requiring a higher time period for this stabilization.

7 Specimens located nearer to the panel's corner showed a higher increase of creep coefficient with time. This aspect
8 could be ascribed to the decrease of the concrete flow velocity with the increase of the distance from the casting
9 point which leads to different fibre distribution as well as matrix constituents through the panel.

10 The creep tests also revealed that the SFRSCC was influenced by the orientation of the notch plane regarding the
11 expected concrete flow (defined by the β angle). In fact, $\beta=[0-15^\circ[$ specimens presented the highest creep
12 coefficients, whereas $\beta=[75-90^\circ]$ series showed the lowest ones. This fact was a direct consequence of the fibre
13 orientation within the panel.

14 In general, the post-cracking strength after the long-term loading was not influenced significantly when compared to
15 the one obtained from instantaneous monotonic tests, even when the specimens were pre-cracked up to close the
16 CTOD corresponding to the maximum load at post-cracking branch, and when loaded with the higher F_a / F_{cr} ratios.

17 Based on the results obtained from the creep tests, an equation was proposed to predict the creep coefficient for the
18 developed SFRSCC when cracked up to 0.5 mm and loaded in the interval $0.5 < F_a / F_{cr} \leq 1.0$.

19 **ACKNOWLEDGEMENTS**

20 This work is supported by the FEDER funds through the Operational Program for Competitiveness Factors -
21 COMPETE and National Funds through FCT - Portuguese Foundation for Science and Technology under the project
22 SlabSys-HFRC-PTDC/ECM/120394/2010. The authors would like to acknowledge the materials supplied by
23 Radmix and Maccaferri (fibres), SECIL (cement), SIKA and BASF (superplasticizers), Omya Comital (limestone
24 filler), and Pegop (Fly ash).

1 APPENDIX A: IMAGE ANALYSIS PROCEDURE

2 The adopted procedure for fibre detection comprised four main steps. Firstly, the fracture surface of the specimen
3 was grinded. Secondly, an RGB image of this surface was taken using a high resolution digital photograph camera.
4 Afterwards, the obtained image was processed using ImageJ [40] software to recognize steel fibres. These steps are
5 depicted in Fig. 20. After analyzing the images, the acquired data was processed and the parameters herein presented
6 were determined.

7 1) The number of fibres per unit area, N^f , is the ratio between the total number of fibres counted in an image, N_T^f
8, (counting all the visible ellipses and circles at the cross section) and the total area of the image, A :

$$9 \quad N^f = N_T^f / A \quad (\text{A.1})$$

10 2) The orientation factor, η_θ , can be regarded as an average orientation towards a certain plane:

$$11 \quad \eta_\theta = \frac{1}{N_T^f} \cdot \sum_{i=1}^{N_T^f} \cos \theta_i \quad (\text{A.2})$$

12 where θ is the out-plane angle that is defined as the angle between the fibre's longitudinal axis and a vector
13 orthogonal to the plane.

14 3) The fibre segregation parameter along the gravity direction, determined from:

$$15 \quad \xi_{seg} = \frac{1}{h \cdot N_T^f} \cdot \sum_{i=1}^{N_T^f} \bar{y} \quad (\text{A.3})$$

16 where \bar{y} is the coordinate in the Y axis of the centre of gravity of the fibre, and h is the height (or depth) of the
17 analysed cross-section. On the other hand, an average value of the coordinates in the Y axis of entire fibres should
18 be determined in the analysed cross-section.

1 REFERENCES

- 2 [1] A. Abrishambaf, J.A.O. Barros, V.M.C.F. Cunha, Relation between fibre distribution and post-cracking
3 behaviour in steel fibre reinforced self-compacting concrete panels, *Cem. Concr. Res.* 51 (2013) 57-66.
- 4 [2] L. Ferrara, A. Meda, Relationships between fibre distribution, workability and the mechanical properties of
5 SFRC applied to precast roof elements, *Mater. Struct.* 39 (2006) 411-420.
- 6 [3] S.T. Kang, J.K. Kim, The relation between fibre orientation and tensile behavior in an ultra high performance
7 fiber reinforced cementitious composite (UHPRCC), *Cem. Concr. Res.* 41 (2011) 1001-1014.
- 8 [4] J.A.O. Barros, J.A. Figueiras, Flexural behaviour of SFRC: Testing and modelling, *ASCE J. Mater. Civ. Eng.* 11
9 (1999) 331-339.
- 10 [5] F. Bencardino, L. Rizzuti, G. Spadea, R.N. Swamy, Experimental evaluation of fibre reinforced concrete fracture
11 properties, *Compos. Part B.* 41 (2010) 17-24.
- 12 [6] S. Carmona, A. Aguado, New model for the indirect determination of the tensile stress-strain curve of concrete
13 by means of the Brazilian test, *Mater. struct.* 45 (2012) 1473-1485.
- 14 [7] E. Denneman, E.P. Kearsley, A.T. Visser, Splitting tensile test for fibre reinforced concrete, *Mater. Struct.* 44
15 (2011) 1441-1449.
- 16 [8] M. Prisco, L. Ferrara, M.G.L. Lamperti, Double edge wedge splitting (DEWS): an indirect tension test to
17 identify post-cracking behaviour of fibre reinforced cementitious composites, *Mater. Struct.* 46 (2013) 1893-1918.
- 18 [9] W.B. Boshoff, V. Mechtcherine, G.P.A.G. van Zijl, Characterizing the time-dependant behaviour on the single
19 fibre level of SHCC: Part 1: Mechanism of fibre pull-out creep, *Cem. Concr. Res.* 39 (2009) 779-786.
- 20 [10] S.E. Arango, P. Serna, J.R. Marti-Vargs, A test method to characterize flexural creep behaviour of pre-cracked
21 FRC specimens, *Exp. Mech. J.* 52 (2012) 1067-1078.
- 22 [11] T. Kanstad, G. Zirgulis, Long-term creep testing of pre-cracked fibre reinforced concrete beams, 8th RILEM
23 International Symposium on Fibre Reinforced Concrete: Challenges and Opportunities, Guimarães, Portugal, 2012.
- 24 [12] L. MacKay, J.F. Trottier, Post-crack creep behavior of steel and synthetic FRC under flexural loading,
25 *Shotcrete: More Engineering Developments*, Taylor and Francis Group, London, 2004.
- 26 [13] K.H. Tan, M.K. Saha, Ten year study on steel fibre-reinforced concrete beams under sustained loads, *ACI*
27 *Struct. J.* 102 (2005) 472-480.

- 1 [14] R.I. Zerbino, B.E. Barragan, Long-term behaviour of cracked steel fibre-reinforced concrete beams under
2 sustained loading, *ACI Mater. J.* 109 (2012) 215-224.
- 3 [15] W.A. Al-Khaja, Mechanical properties and time-dependent deformation of polypropylene fibre reinforced
4 concrete, *J King Saud Univ. Eng. Sci.* 7 (1995) 67-76.
- 5 [16] S. Kurt, P. Balaguru, Post crack creep of polymeric fibre-reinforced concrete in flexure, *Cem. Concr. Res.* 30
6 (2000) 183-190.
- 7 [17] B.H. Oh, D.G. Park, J.C. Kim, Y.C. Choi, Experimental and theoretical investigation on the postcracking
8 inelastic behaviour of synthetic fibre reinforced concrete beams, *Cem. Concr. Res.* 35 (2005) 384-392.
- 9 [18] A.J. Babafemi, W.P. Boshoff, Tensile creep of macro-synthetic fibre reinforced concrete (MSFRC) under uni-
10 axial tensile loading, *Cem. Concr. Compos.* 55 (2014) 62-69.
- 11 [19] C.J. Mouton, W.P. Boshoff, Initial study on the tensile creep of cracked steel fibre reinforced concrete, 8th
12 RILEM International Symposium on Fibre Reinforced Concrete: Challenges and Opportunities, Guimarães,
13 Portugal, 2012.
- 14 [20] G. Zhao, M. di Prisco, L. Vandewalle, Experimental research on uni-axial tensile creep behaviour of pre-
15 cracked steel fibre reinforced concrete, 8th RILEM International Symposium on Fibre Reinforced Concrete:
16 Challenges and Opportunities, Guimaraes, Portugal, 2012.
- 17 [21] K.H. Tan, P. Paramasivan, K.C. Tan, Creep and shrinkage deflections of RC beams with steel fibres, *Mater.*
18 *Civ. Eng.* 6 (1994) 474-494.
- 19 [22] B. Boulekbache, M. Hamrat, M. Chemrouk, S. Amziane, Flowability of fibre-reinforced concrete and its effect
20 on the mechanical properties of the material, *Constr. Build. Mater.* 24 (2010) 1664-1671.
- 21 [23] L. Martinie, N. Roussel, Simple tools for fiber orientation prediction in industrial practice, *Cem. Concr. Res.* 41
22 (2011) 993-1000.
- 23 [24] CEB-FIP, Volume 1, Model Code 2010, Tomas Telford, Lausanne, Switzerland, 2012.
- 24 [25] UNI11039, Steel fibre reinforced concrete, Part I: Definition, classification, specification and conformity, Part
25 II: Test method for measuring first crack strength and ductility indexes, Italian Board for Standardization, 2003.
- 26 [26] EFNARC, The European guidelines for self-compacting concrete, 2005.
- 27 [27] R.M. Lameiras, J.A.O. Barros, I. Valente, M.A.D. Azenha, Development of load-bearing insulated panels
28 combining steel fibre reinforced self-compacting concrete layers and glass fibre reinforced polymer

1 connectors – part I: conception and pull-out tests, *Compos. Struct. J.* 105 (2013) 446-459, DOI information:
2 10.1016/j.compstruct.2013.06.015. <http://hdl.handle.net/1822/26229>

3 [28] R.M. Lameiras, J.A.O. Barros, M.A.D. Azenha, I. Valente, Development of load-bearing insulated panels
4 combining steel fibre reinforced self-compacting concrete layers and glass fibre reinforced polymer connectors –
5 part II: numerically evaluation of mechanical behaviour, *Compos. Struct. J.* 105 (2013) 460-470, DOI information:
6 10.1016/j.compstruct.2013.06.015. <http://hdl.handle.net/1822/26225>

7 [29] S.J. Barnett, J.F. Lataste, T. Parry, S.G. Millard, M.N. Soutsos, Assessment of fibre orientation in ultra-high
8 performance fibre reinforced concrete and its effect on flexural strength, *Mater. Struct.* 43 (2010) 1009-1023.

9 [30] V.M.C.F. Cunha, Steel fibre reinforced self-compacting concrete-from micromechanics to composite
10 behaviour, Civil Engineering Department, University of Minho, Portugal, 2010.

11 [31] L. Ferrara, N. Ozyurt, M. di Prisco, High mechanical performance of fiber reinforced cementitious composites -
12 the role of casting-flow induced fiber orientation, *Mater. Struct.* 44 (2011) 109-128.

13 [32] A. Abrishambaf, J.A.O. Barros, V.M.C.F. Cunha, A state of art study on the fibre orientation and distribution in
14 steel fibre reinforced concrete, University of Minho, Portugal, 13-DEC/E-16, 2013.

15 [33] C.V.S. KamerwaraRao, Effectiveness of random fibres in composites, *Cem. Concr. Res.* 9 (1979) 685-693.

16 [34] P. Stroeven, J. Hu, Effectiveness near boundaries of fibre reinforcement in concrete, *Mater. Struct.* 39 (2006)
17 1001-1013.

18 [35] A. Abrishambaf, J.A.O. Barros, V.M.C.F. Cunha, Determination of time-dependent behaviour of bond in steel
19 fibre reinforced self-compacting concrete, University of Minho, Portugal, 14-JUL/E-18, 2014.

20 [36] A. Abrishambaf, J.A.O., Barros, V.M.C.F. Cunha, Characterizing the time-dependent behaviour of cracked
21 steel fibre reinforced self-compacting concrete panels, University of Minho, Portugal, 14-July/E-19, 2014.

22 [37] EN1992-1-1, Eurocode 2: Design of concrete structures, European Committee of standardization, Brussels,
23 2004.

24 [38] ACI-Committee-209, Prediction of creep, shrinkage and temperature effects in concrete structures, ACI Manual
25 of concrete practice, Part 1, 1997.

26 [39] CEB-FIP, Model code for concrete structures: Evaluation of the time dependent behaviour of concrete, Comite
27 European du Beton/Federation Internationale de la Precontrainte, Lausanne Bulletin d'Information No. 199, , 1999.

28 [40] W. Rasband, ImageJ, National Institutes of Health, USA, 2008.<http://rsb.info.nih.gov/ij/>

FIGURES AND TABLES

1

2 **List of Figures:**

3 Fig. 1: (a) Specimen's extracting plane, (b) definition of β angle.

4 Fig. 2: Test setup of monotonic four-point bending test (dimensions are in mm): (a) geometry of the specimen and
5 LVDT for measuring the deflection (b) LVDTs to record CTOD, (c) LVDT connection details for measuring
6 CTOD.

7 Fig. 3: Creep test setup: (a) general view, (b) position and connection details of the LVDT.

8 Fig. 4: Definition of crack opening parameters in creep test: (a) crack opening- time relationship, $w-t$, (b) force-crack
9 opening curve, $F-w$.

10 Fig. 5: A graphical representation of assembled long-term force-crack width curve.

11 Fig. 6: Location of the plane surface in studied beams (dimensions are in mm).

12 Fig. 7: Explanation for fibre alignment in flowing concrete of a panel: (a) casting from the centre (top view), (b)
13 through the cross section.

14 Fig. 8: Predicted orientation probability functions for β in the intervals: (a) $[0-15^\circ]$, (b) $[15-45^\circ]$, (c) $[45-75^\circ]$ and (d)
15 $[75-90^\circ]$.

16 Fig. 9: Monotonic force-crack tip opening displacement relationship for β in the intervals: (a) $[0-15^\circ]$, (b) $[15-45^\circ]$,
17 (c) $[45-75^\circ]$ and (d) $[75-90^\circ]$; (e) comparison of monotonic F -CTOD relationship for different series.

18 Fig. 10: Crack opening rate as a function of F_a / F_{cr} : (a) specimens pre-cracked up to 0.3 mm, $w_{cr}=0.3$ mm, (b)
19 specimens pre-cracked up to 0.5 mm, $w_{cr}=0.5$ mm.

20 Fig. 11: Relationship between creep coefficient in creep stage and F_a / F_{cr} : (a) $w_{cr}=0.3$ mm, (b) $w_{cr}=0.5$ mm.

21 Fig. 12: Creep coefficient versus time in the creep tests for the two pre-crack width levels grouped in low and high
22 F_a / F_{cr} ratio.

23 Fig. 13: Creep coefficient versus time for specimens at different distances from casting point in the series of: (a)
24 $w_{cr}=0.3$ mm, (b) $w_{cr}=0.5$ mm.

1 Fig. 14: Creep coefficient versus time for different orientation of the notched plane in the series of: (a) $w_{cr}=0.3$ mm,
2 (b) $w_{cr}=0.5$ mm.

3 Fig. 15: Relationship between secondary stiffness, K_{sec} , and long-term residual crack opening width, w_{lt}^{res} .

4 Fig. 16: Comparison of the monotonic and long-term assembled curves for $w_{cr}=0.3$ mm: (a), (b) $\beta = [0-15^\circ]$; (c), (d)
5 $\beta = [15-45^\circ]$; (e), (f) $\beta = [45-75^\circ]$; (g), (h) $\beta = [75-90^\circ]$. (a), (c), (e), (g) $50\% \leq F_a / F_{cr} \leq 75\%$ and (b), (d), (f), (h)
6 $75\% < F_a / F_{cr} \leq 100\%$.

7 Fig. 17: Comparison of the monotonic and long-term assembled curves for $w_{cr}=0.5$ mm: (a), (b) $\beta = [0-15^\circ]$; (c), (d)
8 $\beta = [15-45^\circ]$; (e), (f) $\beta = [45-75^\circ]$; (g), (h) $\beta = [75-90^\circ]$. (a), (c), (e), (g) $50\% \leq F_a / F_{cr} \leq 75\%$ and (b), (d), (f), (h)
9 $75\% < F_a / F_{cr} \leq 100\%$.

10 Fig. 18: Comparison between experimental and analytical creep coefficient vs. time relationship for series: (a)
11 $w_{cr}=0.3$ mm and (b) $w_{cr}=0.5$ mm.

12 Fig. 19: Influence of F_a / F_{cr} load level on the long-term crack opening vs. time response for w_{cr} equal to: (a) 0.3 mm
13 and (b) 0.5 mm.

14 Fig. 20: Image processing steps: (a) converting a RGB image to greyscale image (b) adjusting a threshold, (c)
15 defining mask, noise (remove small noises) and watershed (separated fibres which are stuck together) functions, (d)
16 fitting the best ellipse to each fibre.

17

18

19

20

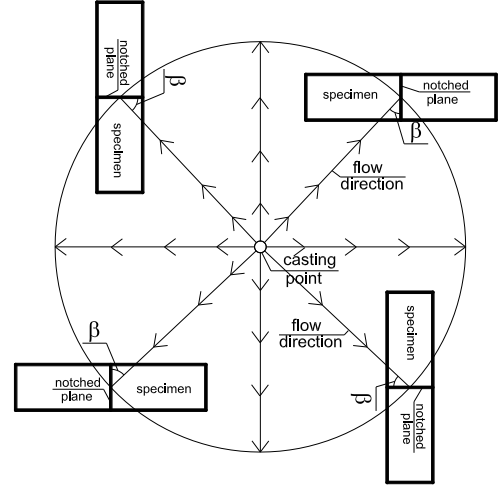
21

22

23

		1500 mm																															
		1500 mm			H-60°-1		H-60°-2		H-60°-3		H-60°-4		A-87.5°-1		A-87.5°-2		A-87.5°-3		A-87.5°-4		A-7.5°-5		H-30°-5										
			H-0.3-60°-5		H-0.3-60°-6		H-0.3-60°-7		H-0.3-60°-8		A-87.5°-29		A-87.5°-30		A-87.5°-31		A-87.5°-32		L-7.5°-5		L-7.5°-6		L-7.5°-7		L-7.5°-8								
		A-0.3-30°-1		A-0.3-30°-3		A-0.3-30°-4		L-0.3-87.5°-5		L-0.3-87.5°-6		L-0.3-87.5°-7		L-0.3-87.5°-8		L-7.5°-9		L-7.5°-10		L-7.5°-11		L-7.5°-12		H-30°-9		H-30°-10		H-30°-11		H-30°-12			
		A-0.3-60°-1		A-0.3-60°-2		L-0.3-7.5°-1		L-0.3-7.5°-2		L-0.3-7.5°-3		L-0.3-7.5°-4		L-7.5°-13		L-7.5°-14		L-7.5°-15		L-7.5°-16		A-7.5°-9		A-7.5°-10		A-7.5°-11		A-7.5°-12					
		A-7.5°-25		A-7.5°-26		A-7.5°-27		A-7.5°-28		A-0.5-60°-5		A-0.5-60°-6		A-0.5-60°-7		A-0.5-60°-8		L-0.5-7.5°-5		L-0.5-7.5°-6		L-0.5-7.5°-7		L-0.5-7.5°-8		H-60°-13		H-60°-14		H-60°-15		H-60°-16	
		H-0.3-30°-1		H-0.3-30°-2		H-0.3-30°-3		H-0.3-30°-4		L-0.5-87.5°-1		L-0.5-87.5°-2		L-0.5-87.5°-3		L-0.5-87.5°-4		A-0.5-60°-1		A-0.5-60°-2		A-0.5-60°-3		A-0.5-60°-4		A-0.5-60°-5		A-0.5-60°-6		A-0.5-60°-7		A-0.5-60°-8	
		H-0.5-30°-5		H-0.5-30°-6		H-0.5-30°-7		H-0.5-30°-8		A-7.5°-21		A-7.5°-22		A-7.5°-23		A-7.5°-24		A-87.5°-17		A-87.5°-18		A-87.5°-19		A-87.5°-20		H-0.5-60°-9		H-0.5-60°-10		H-0.5-60°-11			

(a)



(b)

1

Fig. 1: (a) Specimen's extracting plane, (b) definition of β angle.

2

3

4

5

6

7

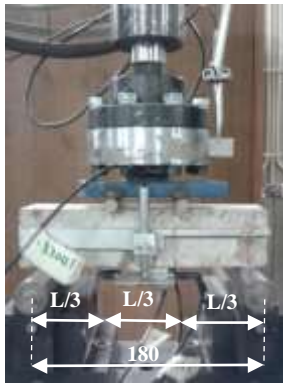
8

9

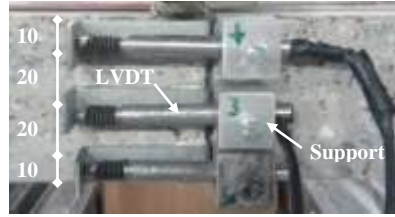
10

11

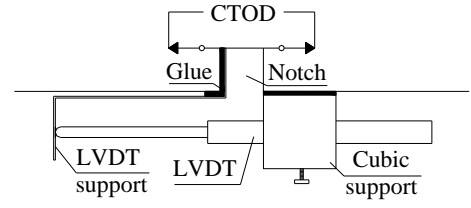
12



(a)



(b)



(c)

1 Fig. 2: Test setup of monotonic four-point bending test (dimensions are in mm): (a) geometry of the specimen and
 2 LVDT for measuring the deflection (b) LVDTs to record CTOD, (c) LVDT connection details for measuring
 3 CTOD.

4

5

6

7

8

9

10

11

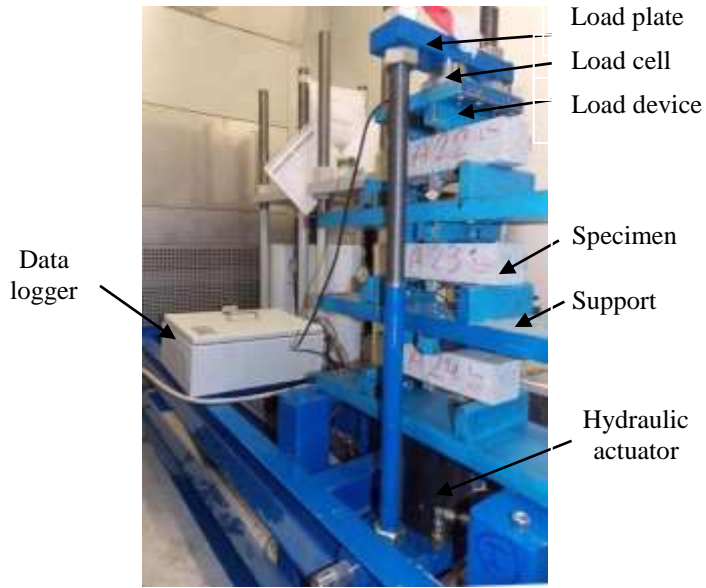
12

13

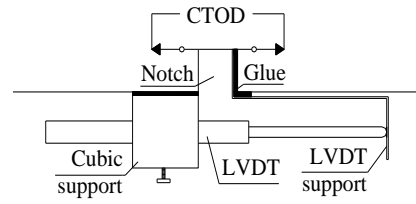
14

15

16



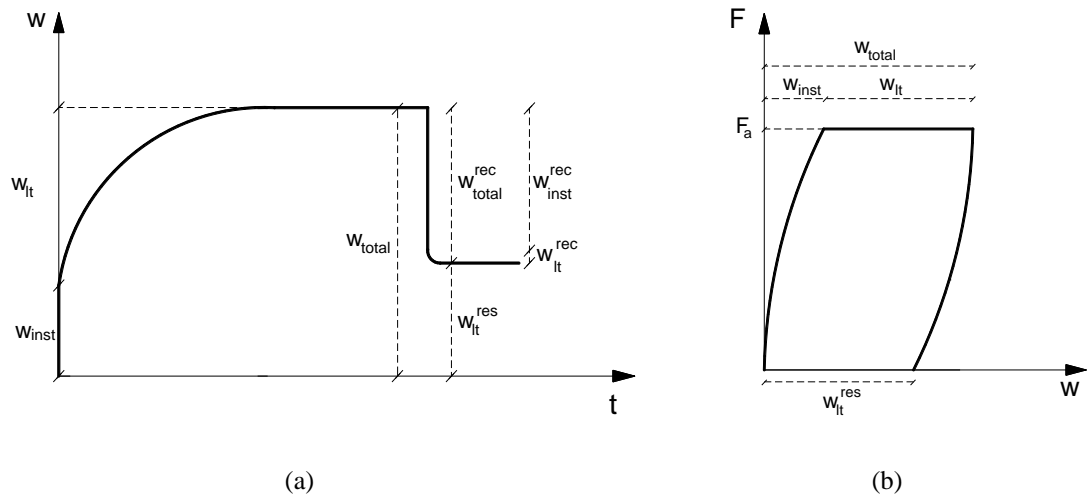
(a)



(b)

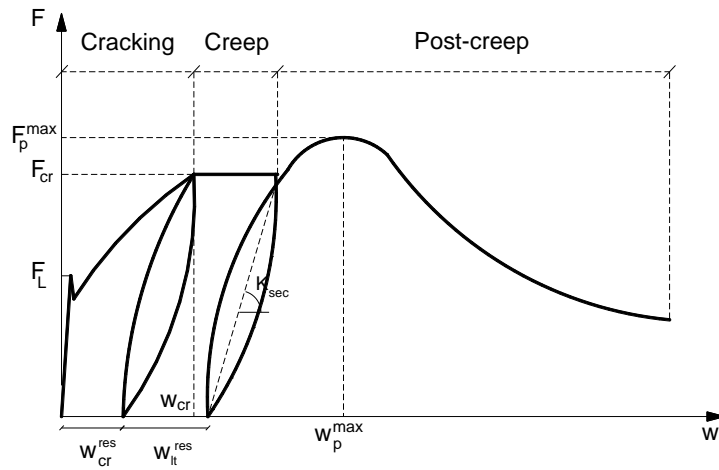
Fig. 3: Creep test setup: (a) general view, (b) position and connection details of the LVDT.

- 1
- 2
- 3
- 4
- 5
- 6
- 7
- 8
- 9
- 10
- 11
- 12
- 13
- 14



1 Fig. 4: Definition of crack opening parameters in creep test: (a) crack opening-time relationship, $w-t$, (b) force-crack
 2 opening curve, $F-w$.

3
 4
 5
 6
 7
 8
 9
 10
 11
 12
 13
 14
 15
 16



1

2

Fig. 5: A graphical representation of assembled long-term force-crack width curve.

3

4

5

6

7

8

9

10

11

12

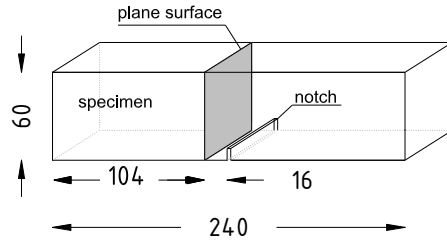
13

14

15

16

17



1

2

Fig. 6: Location of the plane surface in studied beams (dimensions are in mm).

3

4

5

6

7

8

9

10

11

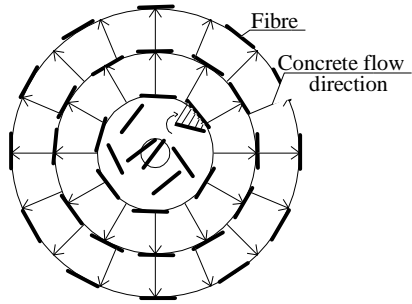
12

13

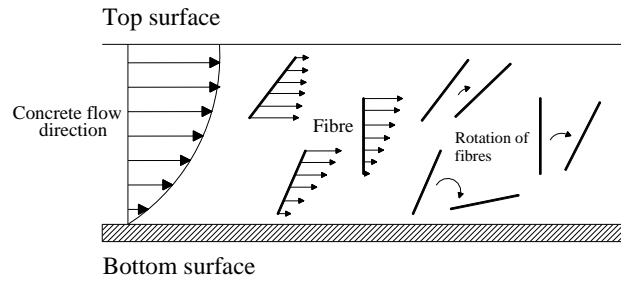
14

15

16



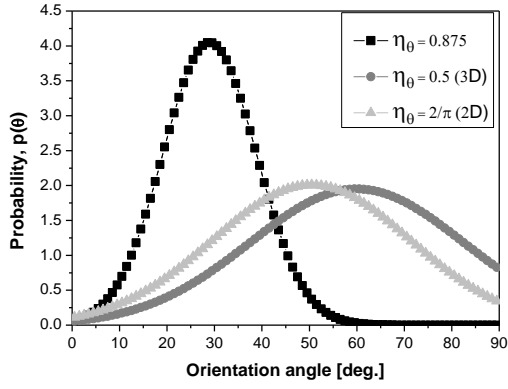
(a)



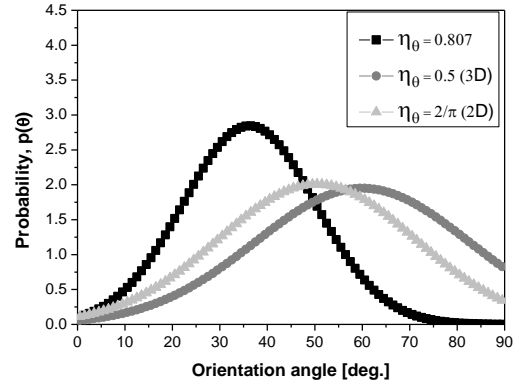
(b)

1 Fig. 7: Explanation for fibre alignment in flowing concrete of a panel: (a) casting from the centre (top view), (b)
 2 through the cross section.

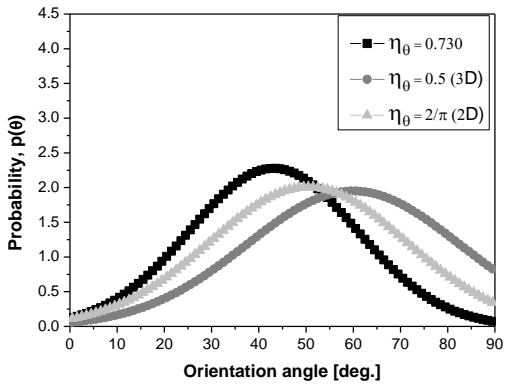
- 3
- 4
- 5
- 6
- 7
- 8
- 9
- 10
- 11
- 12
- 13
- 14
- 15
- 16
- 17



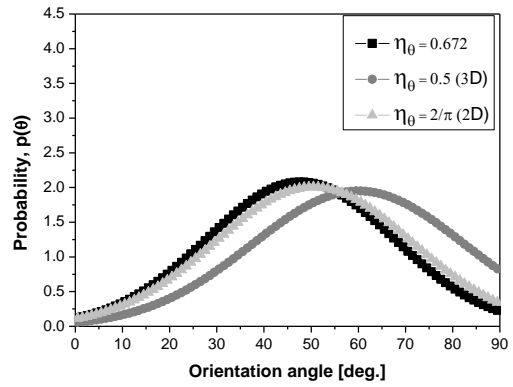
(a)



(b)



(c)



(d)

1 Fig. 8: Predicted orientation probability functions for β in the intervals: (a) $[0-15^\circ]$, (b) $[15-45^\circ]$, (c) $[45-75^\circ]$ and (d)
 2 $[75-90^\circ]$.

3

4

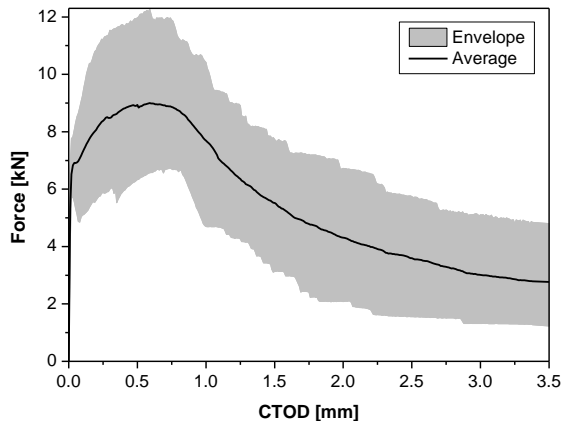
5

6

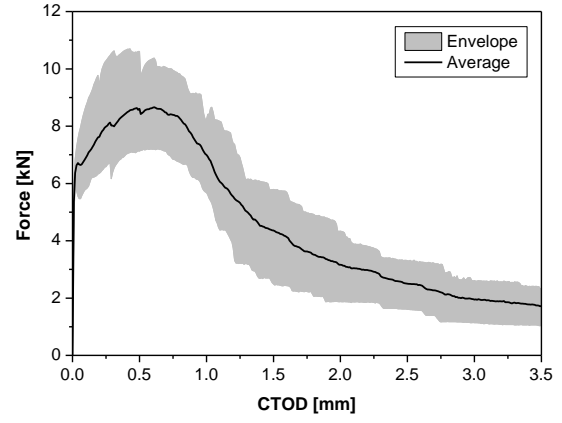
7

8

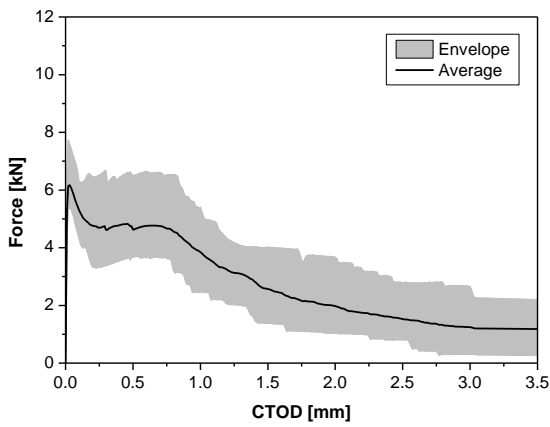
9



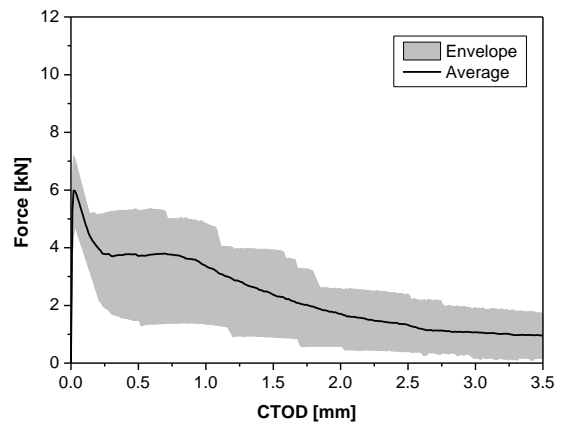
(a)



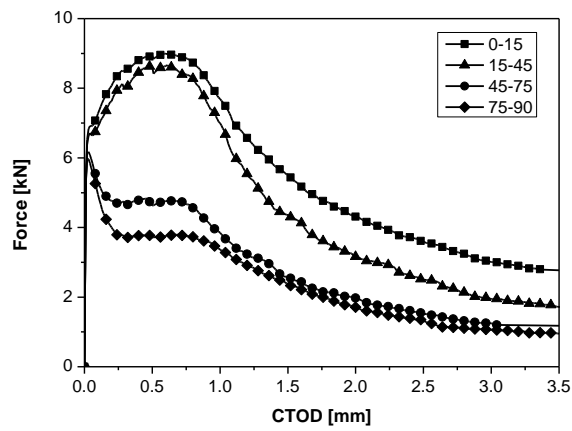
(b)



(c)



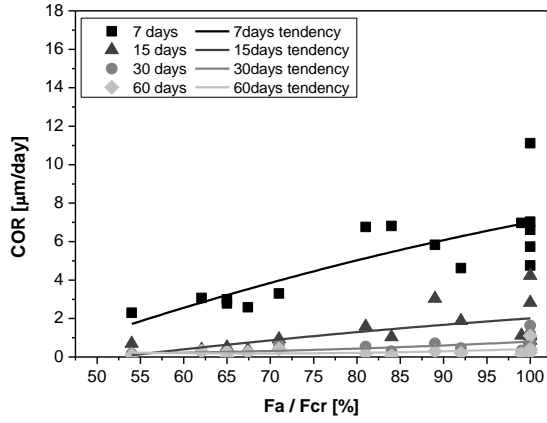
(d)



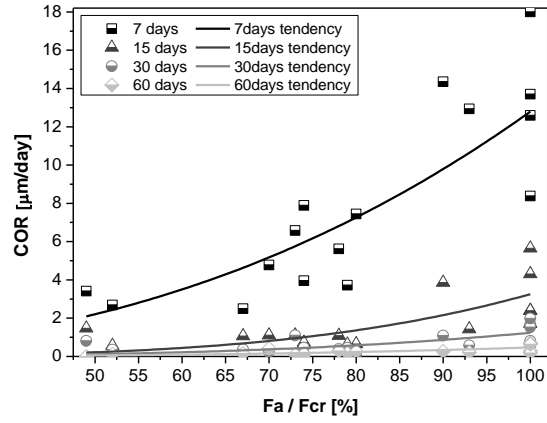
(e)

1 Fig. 9: Monotonic force-crack tip opening displacement relationship for β in the intervals: (a) $[0-15^\circ[$, (b) $[15-45^\circ[$,
 2 (c) $[45-75^\circ[$ and (d) $[75-90^\circ[$; (e) comparison of monotonic F -CTOD relationship for different series.

3



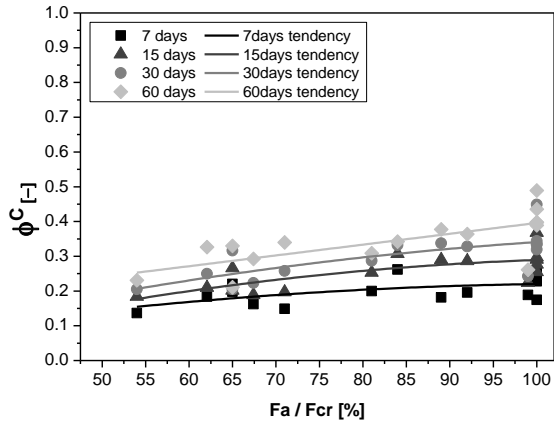
(a)



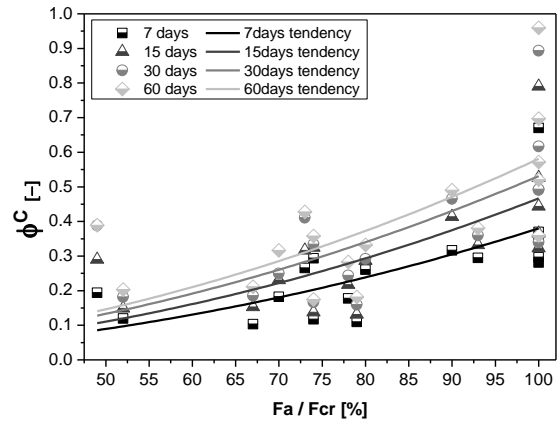
(b)

1 Fig. 10: Crack opening rate as a function of F_a / F_{cr} : (a) specimens pre-cracked up to 0.3 mm, $w_{cr}=0.3$ mm, (b)
 2 specimens pre-cracked up to 0.5 mm, $w_{cr}=0.5$ mm.

- 3
- 4
- 5
- 6
- 7
- 8
- 9
- 10
- 11
- 12
- 13
- 14
- 15



(a)



(b)

1 Fig. 11: Relationship between creep coefficient in creep stage and F_a / F_{cr} : (a) $w_{cr}=0.3$ mm, (b) $w_{cr}=0.5$ mm.

2

3

4

5

6

7

8

9

10

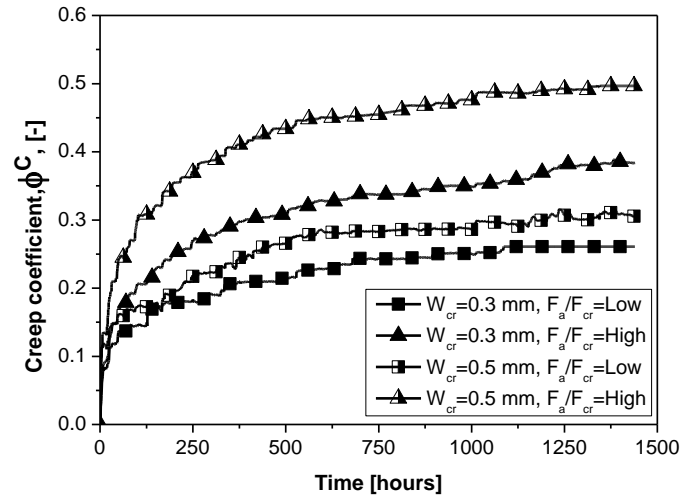
11

12

13

14

15



1

2 Fig. 12: Creep coefficient versus time in the creep tests for the two pre-crack width levels grouped in low and high

3 F_a/F_{cr} ratio.

4

5

6

7

8

9

10

11

12

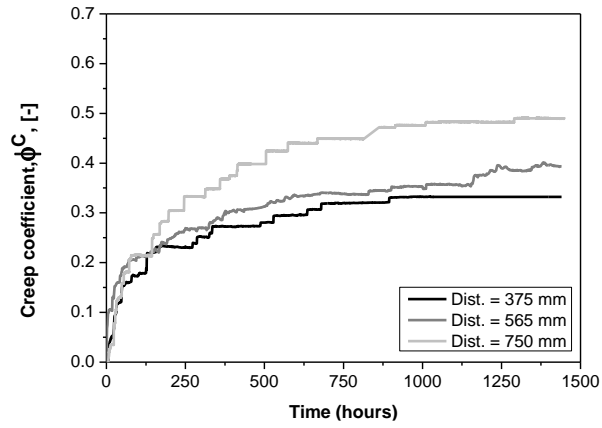
13

14

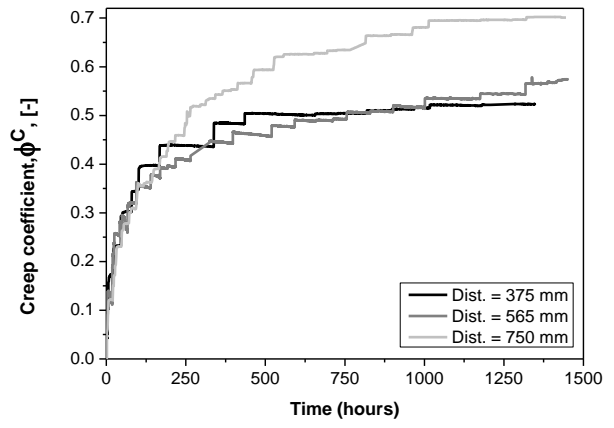
15

16

17



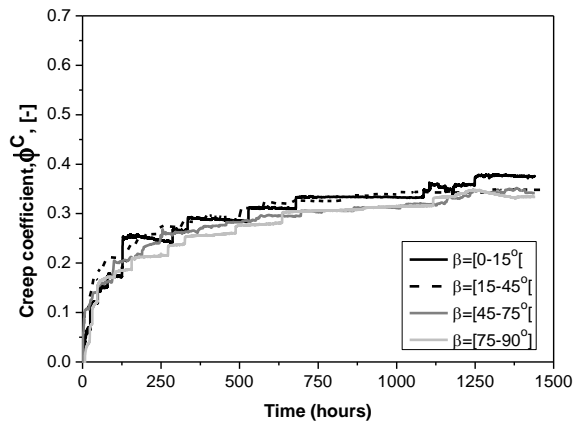
(a)



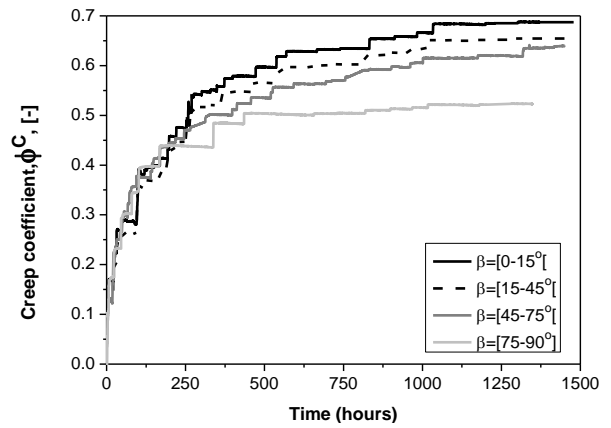
(b)

1 Fig. 13: Creep coefficient versus time for specimens at different distances from casting point in the series of: (a)
 2 $w_{cr}=0.3$ mm, (b) $w_{cr} =0.5$ mm.

- 3
- 4
- 5
- 6
- 7
- 8
- 9
- 10
- 11
- 12
- 13
- 14
- 15
- 16



(a)



(b)

1 Fig. 14: Creep coefficient versus time for different orientation of the notched plane in the series of: (a) $w_{cr}=0.3$ mm,
 2 (b) $w_{cr}=0.5$ mm.

3

4

5

6

7

8

9

10

11

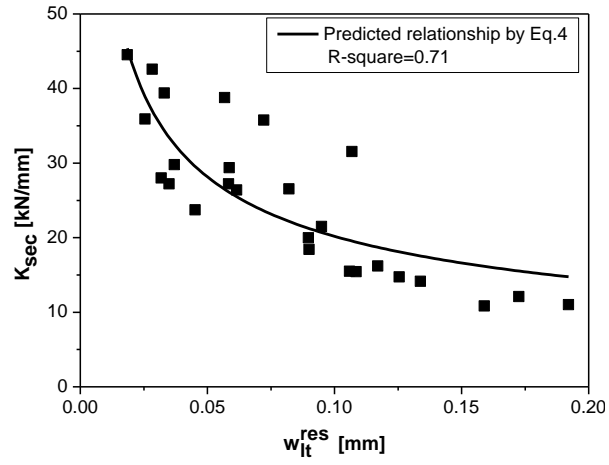
12

13

14

15

16



1

2

Fig. 15: Relationship between secondary stiffness, K_{sec} , and long-term residual crack opening width, w_{lt}^{res} .

3

4

5

6

7

8

9

10

11

12

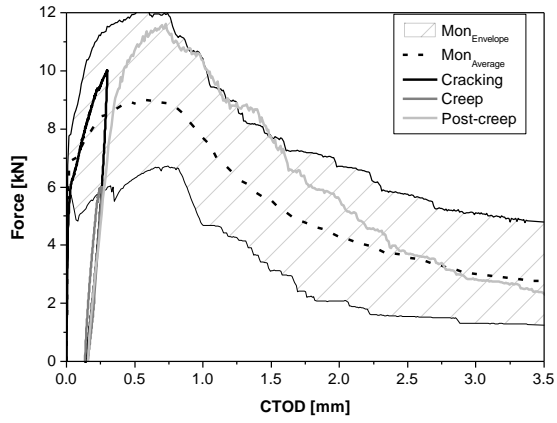
13

14

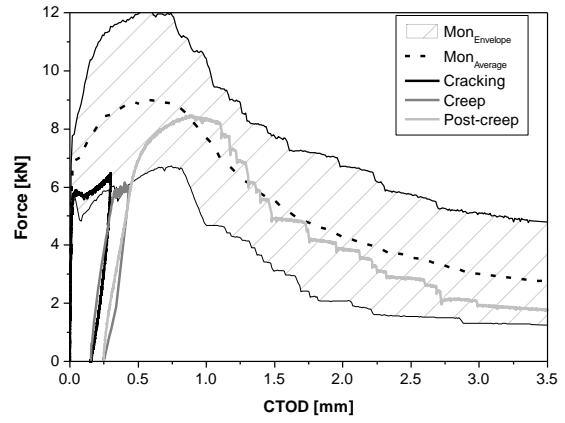
15

16

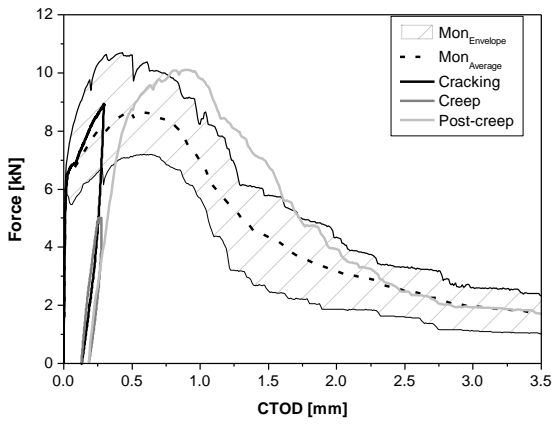
17



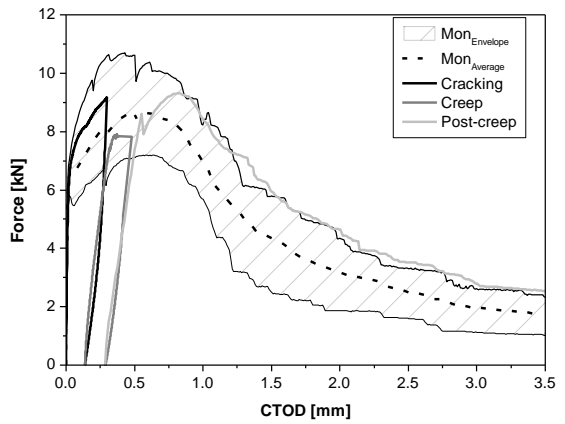
(a)



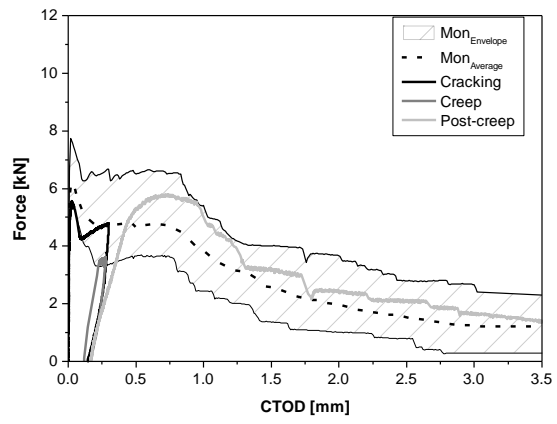
(b)



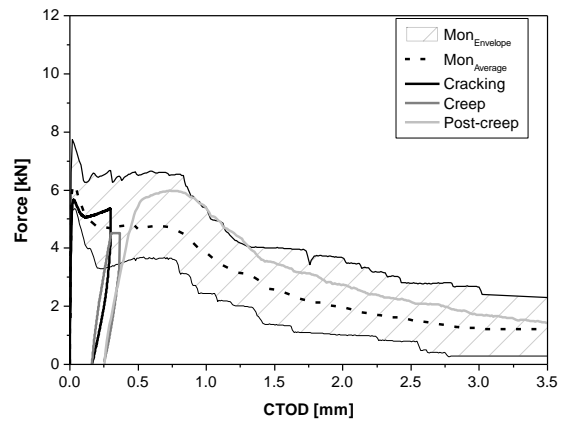
(c)



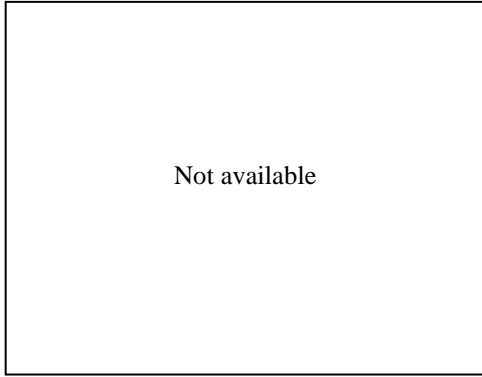
(d)



(e)

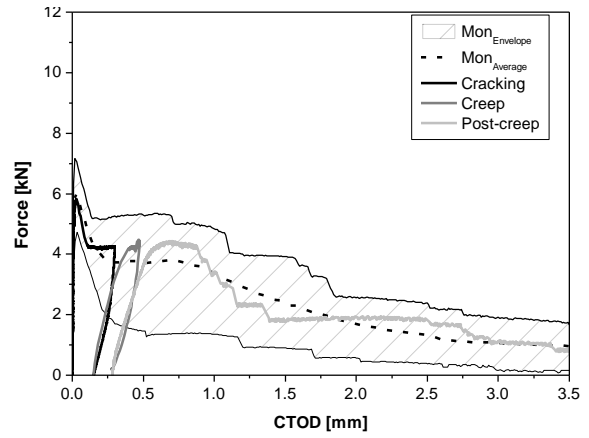


(f)



Not available

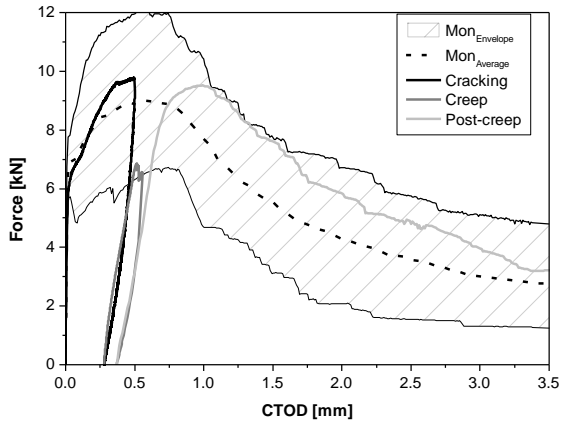
(g)



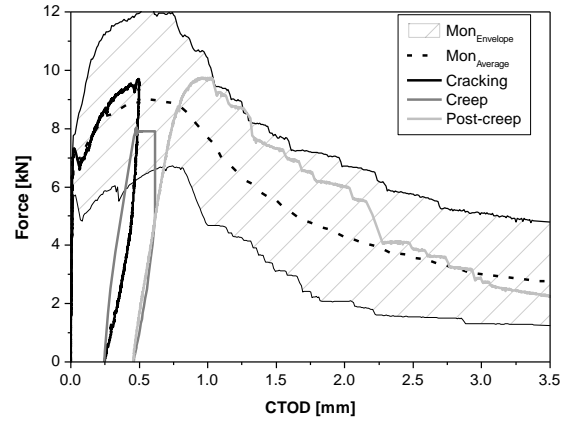
(h)

1 Fig. 16: Comparison of the monotonic and long-term assembled curves for $w_{cr}=0.3$ mm: (a), (b) $\beta = [0-15^\circ]$; (c), (d)
2 $\beta = [15-45^\circ]$; (e), (f) $\beta = [45-75^\circ]$; (g), (h) $\beta = [75-90^\circ]$. (a), (c), (e), (g) $50\% \leq F_a / F_{cr} \leq 75\%$ and (b), (d), (f), (h)
3 $75\% < F_a / F_{cr} \leq 100\%$.

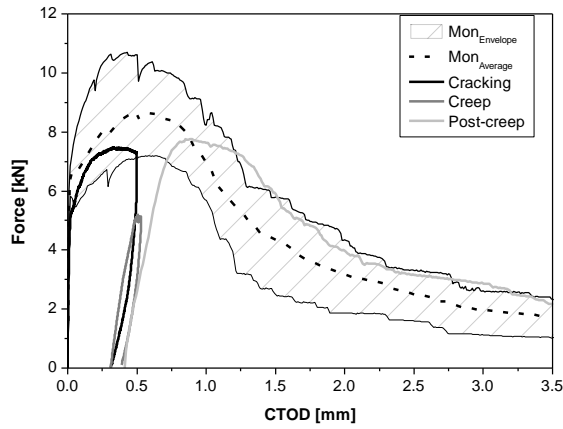
- 4
- 5
- 6
- 7
- 8
- 9
- 10
- 11
- 12
- 13
- 14
- 15
- 16



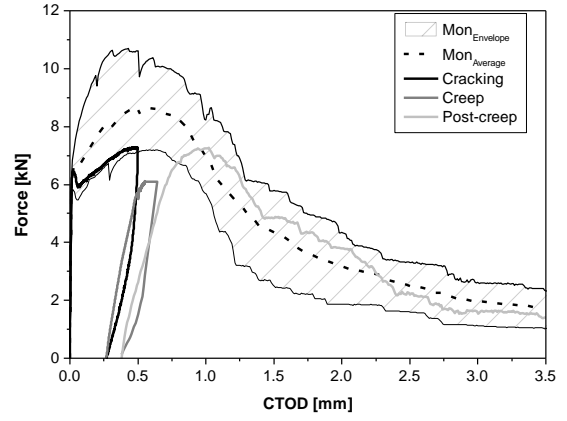
(a)



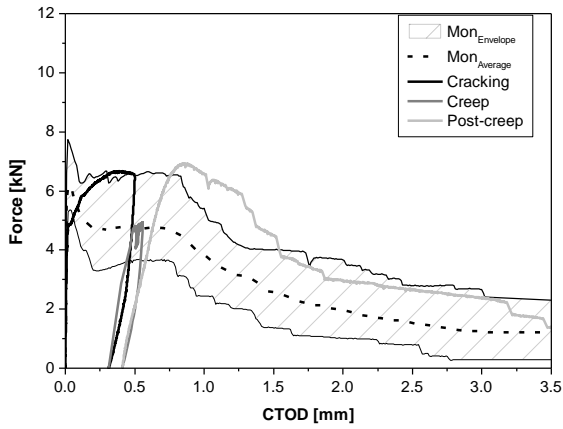
(b)



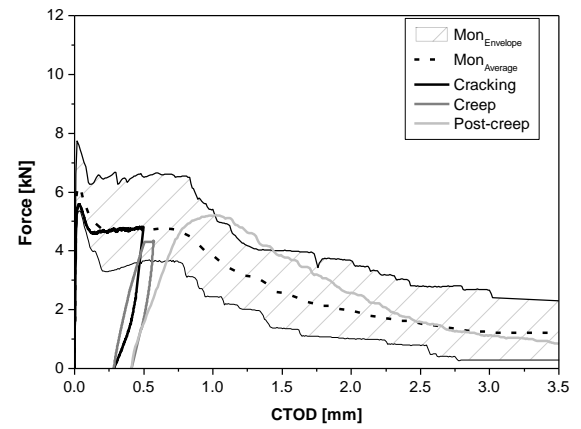
(c)



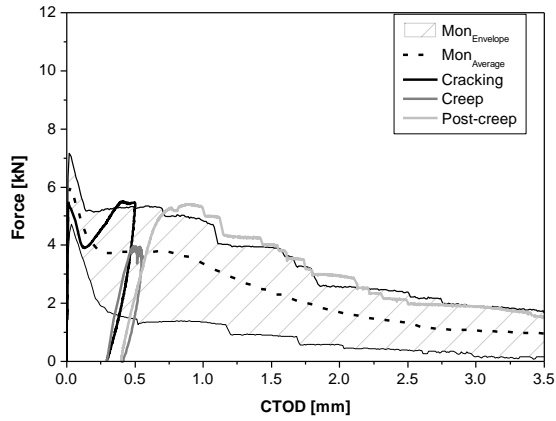
(d)



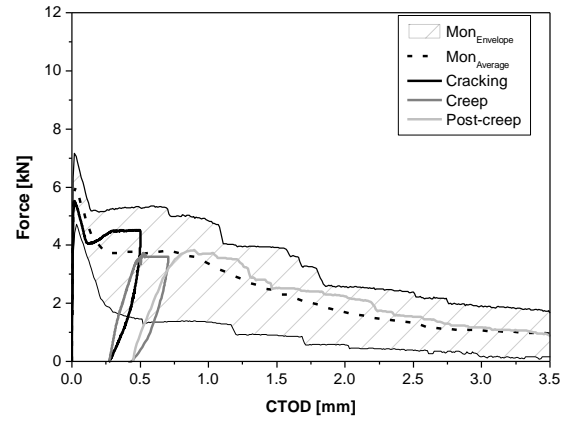
(e)



(f)



(g)



(h)

1 Fig. 17: Comparison of the monotonic and long-term assembled curves for $w_{cr}=0.5$ mm: (a), (b) $\beta = [0-15^\circ]$; (c), (d)
 2 $\beta = [15-45^\circ]$; (e), (f) $\beta = [45-75^\circ]$; (g), (h) $\beta = [75-90^\circ]$. (a), (c), (e), (g) $50\% \leq F_a / F_{cr} \leq 75\%$ and (b), (d), (f), (h)
 3 $75\% < F_a / F_{cr} \leq 100\%$.

4

5

6

7

8

9

10

11

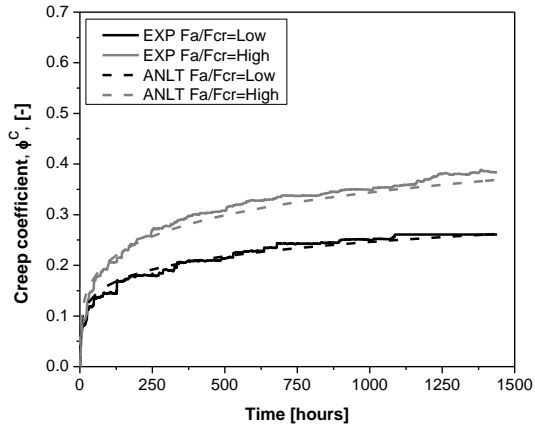
12

13

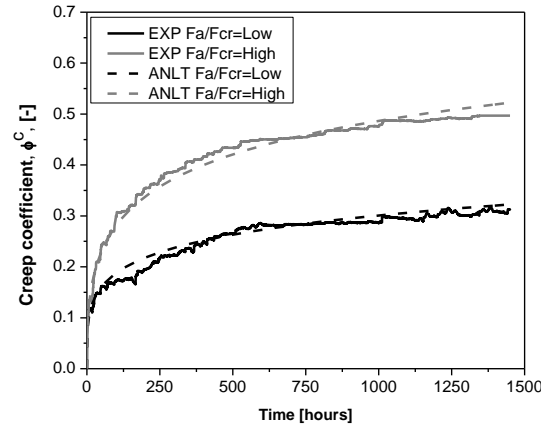
14

15

16



(a)



(b)

1 Fig. 18: Comparison between experimental and analytical creep coefficient vs. time relationship for series: (a)
 2 $w_{cr}=0.3$ mm and (b) $w_{cr}=0.5$ mm.

3

4

5

6

7

8

9

10

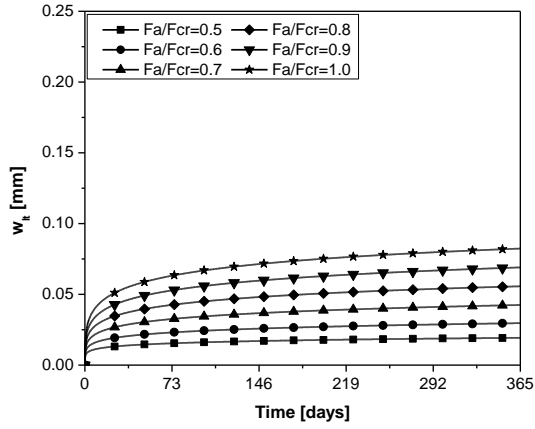
11

12

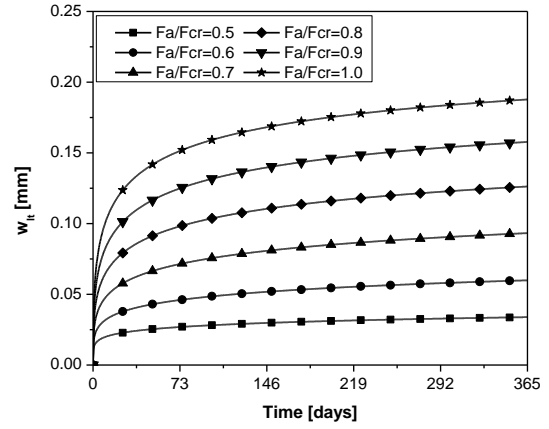
13

14

15



(a)



(b)

1 Fig. 19: Influence of F_a / F_{cr} load level on the long-term crack opening vs. time response for w_{cr} equal to: (a) 0.3 mm
 2 and (b) 0.5 mm.

3

4

5

6

7

8

9

10

11

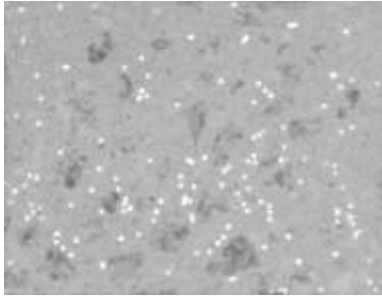
12

13

14

15

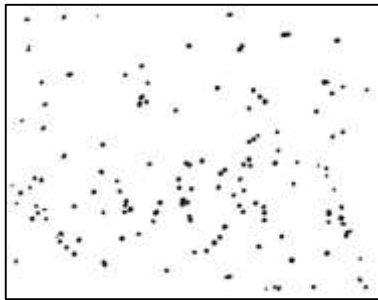
16



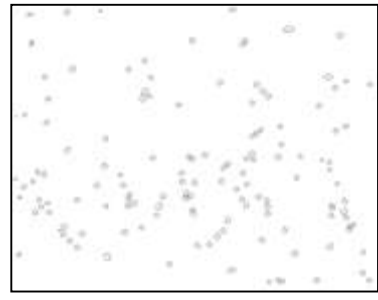
(a)



(b)



(c)



(d)

1 Fig. 20: Image processing steps: (a) converting a RGB image to greyscale image (b) adjusting a threshold, (c)
2 defining mask, noise (remove small noises) and watershed (separated fibres which are stuck together) functions, (d)
3 fitting the best ellipse to each fibre.

4

5

6

7

8

9

10

11

12

1 **List of Tables:**

2 Table 1: Mix design of steel fibre reinforced self-compacting concrete per m³.

3 Table 2: Fibre distribution parameters for the specimens after monotonic 4-P bending test.

4

5

1

Table 1: Mix design of steel fibre reinforced self-compacting concrete per m³.

Cement [kg]	Water [kg]	W/C [-]	SP [kg]	Filler [kg]	Fine sand [kg]	Coarse sand [kg]	Coarse aggregate [kg]	Fibre [kg]
413	124	0.30	7.83	353	237	710	590	60

2

3

4

5

6

7

8

9

10

11

12

13

14

15

16

17

18

19

1

Table 2: Fibre distribution parameters for the specimens after monotonic 4-P bending test.

	Specimen	N^f	N_{eff}^f	η_θ	ξ_{seg}
		[fibres/cm ²]	[fibres/cm ²]	[-]	[-]
$\beta=[0-15^\circ[$	Average	2.12	1.18	0.875	0.52
	CoV (%)	21.11	27.54	1.01	2.50
$\beta=[15-45^\circ[$	Average	1.76	0.67	0.807	0.52
	CoV (%)	11.75	28.65	4.37	2.56
$\beta=[45-75^\circ[$	Average	1.53	0.46	0.73	0.58
	CoV (%)	25.93	19.59	6.36	8.77
$\beta=[75-90^\circ]$	Average	0.87	0.15	0.672	0.62
	CoV (%)	21.75	78.38	12.94	15.21

2

3